NOVEL RF COIL TECHNOLOGIES FOR MRI

A THESIS
SUBMITTED TO THE DEPARTMENT OF ELECTRICAL
AND
ELECTRONICS ENGINEERING
AND THE INSTITUTE OF ENGINEERING AND SCIENCE
OF BILKENT UNIVERSITY
IN PARTIAL FULFILLMENT OF THE REQUIREMENTS
FOR THE DEGREE OF
MASTER OF SCIENCE

By
Haydar Çelik
June, 2006

INVITATION

Galloping from Far Asia and jutting out
into the Mediterranean like a mare's head
this country is ours.

Wrists in blood, teeth clenched, feet bare
and this soil spreading like a silk carpet,
this hell, this paradise is ours.

Shut the gates of plutocracy, don't let them open again,
annihilate man's servitude to man,
this invitation is ours..

To live like a tree single and at liberty
and brotherly like the trees of a forest,
this yearning is ours.

Nazım Hikmet Ran

I certify that I have read this thesis and that in my opinion it is fully adequate, in scope and in quality, as a thesis for the degree of Master of Science.

Prof. Dr. Ergin Atalar (Supervisor)

I certify that I have read this thesis and that in my opinion it is fully adequate, in scope and in quality, as a thesis for the degree of Master of Science.

Prof. Dr. Ayhan Altıntaş

I certify that I have read this thesis and that in my opinion it is fully adequate, in scope and in quality, as a thesis for the degree of Master of Science.

Prof. Dr. Turgut Talı

Approved for the Institute of Engineering and Sciences:

Prof. Dr. Mehmet B. Baray
Director of Institute of Engineering and Sciences

ABSTRACT

NOVEL RF COIL TECHNOLOGIES FOR MRI

Haydar Çelik

M.S. in Electrical and Electronics Engineering

Supervisor: Prof. Dr. Ergin Atalar

June, 2006

In this thesis, we investigated five novel radiofrequency (RF) coil technologies for their use in Magnetic Resonance Imagers. These studies were grouped into two: the first group was on RF coil technologies for interventional MRI; the second group was on the design of optimally performing coils. As a result of these studies, one journal paper was published, one other paper had been submitted, and five abstracts were presented in international meetings.

Interventional MRI is the technology that guides surgical procedures by the aid of magnetic resonance images. One of the topics of interest in interventional MRI is to determine the position of devices used during the interventions. Recently, use of inductively coupled RF (ICRF) coils had been proposed for this purpose. Our first group of studies was on development of novel technologies by using these ICRF coils. In the first study, we proposed a method, which enables separate visualization of the ICRF coil in the body with one color-coded image by utilization of reverse and forward polarization modes of a receive-only (RO) birdcage coil. In the second study, we extended the first study by reformulating the ICRF coil visualization problem for phased array coils. With this, the proposed method became more practical since most of the

modern receive coils are phased array coils. In the third ICRF coil study, use of ICRF coil technology in image-guided neurosurgery was utilized as a registration marker by increasing the signal intensity of gel markers.

Our second group of studies started with calculation of the ultimate achievable signal-to-noise ratio (SNR) using any arbitrary internal coils. This ultimate value later used to test the performance of various internal MRI coils. In the last study, we aimed to solve an inverse problem that is to design a coil that generates SNR close to its ultimate value. First, we determined that a birdcage coil generates the optimum coil sensitivity; however, its z-directed sensitivity should be more localized in the center of the object. For this purpose, we designed and fabricated a microstrip based birdcage coil, which can be used as head coil for 1.5 Tesla MR imagers.

RF coils are critically important in performance of MRI scanners. We believe that studies conducted in this project are contributions toward obtaining better imaging systems.

Key words: RF Coils, Endoluminal RF Coils, SNR in MRI, Interventional MRI; Catheter Tracking; Image guided surgery, Birdcage Coil, Microstrip Based RF Coils,

ÖZET

MANYETİK REZONANS GÖRÜNTÜLEME İÇİN ORİJİNAL RF BOBİN TEKNOLOJİLERİ

Haydar Çelik
Elektrik Elektronik Mühendisliği, Yüksek Lisans
Tez Yöneticisi: Prof Dr. Ergin Atalar
Haziran, 2006

Bu tezde Manyetik Rezonans Görütüleme Aletlerinde kullanılmak üzere beş orijinal radyo frekansı (RF) Bobin teknolojisi üzerine çalıştık. Bu çalışmalar iki gruba ayrılabilir: birincisi girişimsel MRG için RF bobin teknolojileri; ikincisi en iyi çalışan bobin tasarımı. Bu çalışmaların sonucu olarak bir bilimsel makale basıldı, bir diğer çalışma basılması üzere gönderildi ve beş tane özet uluslararası konferanslarda sunuldu.

Girişimsel MRG, manyetik rezonans görüntüleri yardımıyla cerrahi işlemlerin rehberliğini yapma teknolojisidir. Girişimsel MRG'nin konularından biri ameliyat sırasında kullanılan aletlerin yerinin tayinidir. Yakın geçmişte, indüklenerek eşlenmiş radio frekans (İERF) bobinler bu iş için önerilmiştir. Birinci grup çalışmamızda bu İERF bobinler kullanarak original teknolojiler geliştirilmesi üzerinde durduk. İlk çalışmamızda alıcı olarak özel tasarlanmış sadece-alıcı kuşkafesi bobin kullanılarak yeni bir İERF bobbin izleme tekniği önerilmiştir. Bu teknik, sadece-alıcı kuşkafesi bobinin düz ve ters kutuplaşma

kutuplaşma modlarının kullanılmasıyla, kateter ve vücut görütüsünün aynı anda bir renk-kodlu görüntüde gösterilmesine olanak sağlar. İkinci çalışmamızda ilk çalışmamızı tekrar formüle ederek faz dizisi bobinleri üzerine geliştirdik. Bu haliyle yöntem çok daha uygulanabilir olmuştur, çünkü, modern bobinlerin çoğu faz dizisi bobinleridir. Üçüncü İERF bobin çalışmamızda ise, İERF bobin teknolojisinin görüntü-rehberli sinirselcerrahide jel işaretleyicilerinin sinyal seviyesini arttırarak işaretleyici konumlandırıcısı olarak kullanılmıştır.

Ikinci grup çalışmamız dahili manyetik resonans (MR) bobinlerinin kullanılmasıyla elde edilebilecek sinyal/gürültü oranının (SGO) üst sınırı (en iyi içsel sinyal/gürültü oranı, EİİSGO) hesaplanmasıyla başlar. Bu en iyi değer daha sonra farklı dahili MRG bobinlerinin performansını ölçmede kullanılmıştır. Son çalışmamızda ise, en iyiye yakın SGO'yu verecek bobini tasarlamak için ters problemi çözmeyi amaçladık. Öncelikle, kuşkafesi bobininin en iyi hassaslığı yaratabileceğine karar verdik, fakat, bobinin z-yönlü hassaslığı daha çok merkezde yoğunlaşması gerekliydi. Bu amaçla, 1.5 T MR görüntüleyicilerde kafa bobini olarak kullanılabilmesi için mikroşerit temelli kuşkafesi bobini tasarladık ve yaptık.

RF bobinler MRG aletlerinin performanslarında kritik öneme sahiptir. İnanıyoruz ki, daha iyi görüntüleme sistemleri için yaptığımız çalışmaların katkısı olacaktır.

Anahtar Sözcükler: RF Bobinler, Endoluminal Bobinler, MRG'deki SGO, Girişimsel MRG, Kateter İzleme, Görüntü Rehberli Ameliyat, Kuşkafesi Bobini, Mikroşerit Tabanlı RF Bobinleri

ACKNOWLEDGEMENTS

First, I wish to acknowledge my supervisor, **Prof. Ergin Atalar**, without whom I would never have started or finished this work. Beyond his role as a supervisor, he has been a very good friend. Even I have called him after midnight, he has not complained and motivated me excellently.

My special thanks go to Prof.Ayhan Altıntaş and Dr.Vakur Ertürk for their help during my research. I would also like to thank my friends and co-workers, Yiğitcan Eryaman and Kerim Kara. Special mention goes to Prof. Turgut Talı, Serhan Atilla, and Aslı Ulutürk from Gazi University Hospital for their clinical support. I would also like to thank Mürüvet Parlakay for her patience for eight years. I am very grateful for the support that I received from our technicians Ersin Başar and Ergün Hırlakoğlu.

This work dedicated to my parents, Fatma and Hasan, without whom I couldn't be on earth and my brothers, Kenan, Bünyamin, Mustafa, and Barış for their friendship and help in my entire life and my second family Can and Çiğdem Özerdoğan for their continuous support.

Table of Contents:

List of Figures:

Figure 2.6: Visualization process of the ICRF coil and the body. Spins in the body creates a forward polarized signal. If an ICRF coil is placed in the RO birdcage coil, spin rotation induces current on the ICRF coil and it creates linear polarized signal, which consists of both forward and reverse polarized signals. By feeding ***x*** and ***y***-channels directly to the scanner, both forward and reverse polarized modes can be reconstructed.

Figure 2.7: Phantom experiment of the ICRF coil without decoupling diodes. **a)** Reverse polarization mode image. Note that, because of strong decoupling, the image ICRF coil is disturbed. **b)** Forward polarization mode image.

Figure 2.8: Phantom experiment of ICRF coil with decoupling diodes. **a)** Reverse polarization mode image. **b)** Forward polarization mode image. As seen in Figure 2.8a, decoupling diodes increases visibility of the ICRF coil.

Figure 2.9: Rabbit experiment results. We placed a modified naso-gastric tube inside the esophagus of the animal. **a)** Forward polarization mode image. It is difficult to distinguish the ICRF coil from the background. **b)** Reverse polarization mode image. In this mode, ICRF coil clearly visible and background signal is reduced. **c)** The forward and reverse polarized images are combined using color-coding.

Figure 3.1: The inductively coupled RF (ICRF) coil and linear polarization. MR signal induces current on an ICRF coil and this creates a linear polarized signal. A linearly polarized signal can be decomposed into forward and reverse polarized signals. Therefore, an ICRF coil functions as a polarization converter.

Figure 3.2: Schematic representation of acquired image data. Images are 512 X 256 and there are N images from N channels.

Figure 3.3: Flowchart for the case when there is only body image. Sensitivity is directly related to data come from channels.

Figure 3.4: Flowchart for the case when there are both body and catheter images. In order to obtain *c* vector, low-pass filtering of the channel data are required before manipulations.

Figure 3.5: The ICRF coil without decoupling. The ICRF coil has a diameter of 2.1 mm and length of 10 cm. It is constructed from 0.4 mm diameter coated copper wire. The ICRF coil is tuned by a ceramic chip capacitor to 63.85 MHz using an HP 8753D network analyzer.

Figure 3.6: **a)** Forward polarization mode image. **b)** Reverse polarized mode image. **c)** Color-coded image

Figure 3.7: Flowchart for 6-channels phased array coil. In order to obtain reverser polarization mode of image, channel data is multiplied by a proper matrix and they are added up.

Figure 4.1: Different configurations of ICRF coils. **a)** Without capacitor and diode. **b)** With tuning capacitor. **c)** With decoupling diodes. **d)** With single decoupling diode.

Figure 4.2: **a)** The ICRF coil with tuning capacitor and decoupling back-to-back diodes. **b)** Sketch of ICRF coil, MMM, and head of a patient.

Figure 4.3: Multi-Modality (Gel) Markers (IZI Medical Products). Zinreich introduced a gel for image-guided surgery and this marker is used with our ICRF coils.

Figure 4.4: Multi-Modality Marker. As seen in the figure, marker is not clear.

Figure 4.5: Coil-1 with Multi-Modality Marker. ICRF coil increased signal intensity significantly

Figure 4.6: Coil-2 with Multi-Modality Marker. ICRF coil increased signal intensity so that signal near the gel saturates.

Figure 4.7: Coil-1 with Multi-Modality Marker. Marker cannot be seen in this sequence (T2 Weighted Fat Suppression).

Figure 4.8: Coil-1 with Multi-Modality Marker

Figure 4.9: Coil-2 with Multi-Modality Marker.

Figure 5.1:. **a)** Cylindrical body model with a coaxial cavity. This model is used for obtaining the UISNR values of an internal and external coil combination. **b)** A cylindrical body model without a cavity.

Figure 5.2: Signal reception profile of optimum internal coil (axial H-map). This shows the optimum field pattern inside the body model that will maximize the intrinsic SNR at location $(\rho\text{=1 mm}, \phi\text{=0}, \text{ z=0})$. A logarithmic intensity scale is employed.

Figure 5.3: **a)** Sagittal H-map for the optimum coil. This map is produced on the plane, ϕ = 0, and the point of interest located at $(\rho = 1 \text{ mm}, \phi = 0, z = 0)$ is indicated by a star. A logarithmic intensity scale is employed. **b)** Sensitivity magnitude profile for the optimum coil. H_+ field sensitivity is plotted at $x = 1$ mm in arbitrary units. Both figures show that most of the field energy is concentrated in a narrow region on the z axis and the greatest brightness indicates where the position of the internal coil should be.

Figure 5.4: Relative importance of the modes (G-map).This is used for the numerical calculation of the UISNR. The weights of each mode were mapped on the horizontal and vertical axis, representing the *m* and *n* modes. The restriction of the

modes to those encompassed by bound W2 speeds the calculation with a negligible loss of accuracy (< 1%), whereas use of the overly-restrictive bound W1 results in a 33% error.

Figure 5.5: A comparison of three ISNR values. ρ_0 is the radial distance of the point of interest from the center of the object. The internal coil is effective at points near the cavity and then the external coil becomes effective as the point of interest approaches the outer boundary on the curve of the UISNR of an internal and external coil combination. In this figure, the external coil has a 20 cm

Figure 5.6: The useful area for the loopless antenna. The SNR values of the loopless antenna and the UISNR of the internal and external coil combination were compared for different values of body radius, ρ_b. For a given body radius, the loopless antenna outperforms the optimum external coil design for points of interest with ρ_0 values that fall in the shaded area. The region at the left bottom of the figure, shown by the dashed line, was found by interpolation.

Figure 5.7: The performance of the loopless antenna as a function of distance of the point of interest from the center of the object. This figure was obtained by dividing the SNR of the loopless antenna by the UISNR of the internal and external coil combination. In this figure, a 20 cm body radius and a 0.375 mm cavity radius were assumed.

Figure 5.8: The experimental performance of the endourethral coil design as a function of distance of the point of interest from the center of the object. This figure shows the performance of a single-loop endourethral coil obtained by dividing the experimental SNR value of this coil by the UISNR of the internal coil. UISNR values were computed for a 20 cm radius body with an internal cavity radius of 2.5 mm (cavity size matched the endourethral coil diameter).

Figure 5.9: Frequency dependency of the UISNR at various magnetic field strengths. When the point of interest is at a small cylindrical radius, quasi-static conditions are valid and there is then an approximately linear relationship between the UISNR and field strength.

Figure 5.10: The performance of coils with different cavity sizes. In this figure, different UISNR values for internal coils were compared for different cavity sizes. The comparison was made by dividing the UISNR values of various coils, which have different cavity radii, to the UISNR value of the reference coil, which has a cavity radius equal to 0.375 mm

Figure 6.1: Sketch of Microstrip Based Birdcage Coil

Figure 6.2: Another sketch of MSBC.

Figure 6.3: A sketch of microstrip based birdcage coil for 1.5 T.

Figure 6.4: Axiel Image of phantom

Figure 6.5: Coronal Image of phantom

1. INTRODUCTION

From the beginning of the magnetic resonance imaging, RF coils have been very crucial devices of the system. Development acceleration of the RF coils decreased after mid 90's, because research concentration was on the development of novel pulse sequences. However, after the introduction of parallel imaging techniques, such as SENSE (1) and GRAPPA (2), RF coil development re-gained acceleration. This acceleration has been further increased by the strong demand of high performance and specialized RF coils in the field of interventional MRI.

1.1 Interventional MRI

Recently, Zerhouni, Director of National Institute of Health of United States. stated that image guided interventions would be very important in biomedicine in the near future (3). In addition, in ISMRM 2006, it was obvious that interest on the interventional MRI increased sharply as compared to previous years. The reason of this interest originated from the vitality of the interventional MRI. It is expected that in the near future, surgeons will be able to conduct very difficult surgical procedures successfully by the visual aid of MRI during these procedures. Accurate removal of the lesions will be possible while keeping the healthy tissue unharmed. Surgical instruments will be delivered safely into deep locations. One of the current problems in interventional MRI is accurate localization surgical devices such as catheters in the body. Although different methods have been introduced for catheter tracking (4-7), so far the problem has not been solved completely.

In this thesis we have conducted three projects on development of novel inductively coupled RF (ICRF) coil technologies for better device localization. We used a special design receive-only birdcage coil (8) as a receiver and made use of reverse polarization technique to improve wireless active catheter tracking method (7) and it had no limitations such as flip angle and safety. This work is presented in ESMRMB Basel, in 2005 (9), and ISMRM Seattle, in 2006

(10), and submitted to Magnetic Resonance in Medicine as a journal paper. We extended this method to phased array coils as a second study. With this, we eliminated the need of specially designed birdcage coils to generate reverse polarization and the method became applicable to any phased array coil. In our third study, ICRF coil was utilized in localization procedure during image-guided surgery. Among others, Multi-Modality Markers (11) were most widely used registering products. However, in some sequences, these markers were not bright enough making device localization difficult. To solve this problem, we proposed an inductively coupled RF (ICRF) coil, which increases signal intensity of Multi-Modality (Gel) Markers (MMM).

1.2 Optimum RF coil technology

In addition to interventional MRI studies, we have conducted two research projects on development optimum RF coil technologies.

Ocali and Atalar (12) determined the ultimate limits of the intrinsic SNR (ISNR) (13) in an MRI experiment. Recently, Siemens introduced 96 channels body coil system, Total Imaging Matrix (TIM) (14), in order to approach this ISNR limit. On the other hand, internal coils have been developed to increase resolution of esophagus (15), urethra (16), blood vessels (17,18), and rectum (19). However, there was no study on ISNR limitations of internal coils. Is there a room for further improvement in SNR using internal MRI coils?

In our forth study, upper bounds for signal-to-noise ratio (Ultimate Intrinsic Signal-to-Noise Ratio, UISNR) for internal coils were calculated. Furthermore, optimum sensitivity for maximum ISNR was theoretically found for any coil. This work was presented in ISMRM 2004, in Toronto (20), and published in Magnetic Resonance in Medicine in 2004 (21).

As a last study, we aimed to solve an inverse problem, which we introduced in the forth study. In order to design a coil which had an optimum sensitivity profile, results of ultimate ISNR study was utilized, and we determined that a birdcage coil could generate the optimum coil sensitivity.

Therefore, we decided to fabricate a birdcage coil for 1.5 T. This work was presented in APS-URSI, Washington, in 2005 (22) and in IMIM, Istanbul, in 2005 (23).

As stated above, this thesis consists of five different novel RF coil technologies that are grouped into two categories. Starting with first category, the first study, ICRF coil tracking using reverse polarization will be discussed in the next chapter. Chapter 3 will be devoted to the phased array implementation of the ICRF coil tracking technology. Chapter 4 will be on the usage of ICRF coil technology in enhancement of surgical marker signal intensities. We will switch to the second group of studies after Chapter 5. First subject will be on evaluation of internal MRI coils using ultimate intrinsic SNR. The last subject, design and fabrication of micro-strip birdcage coils will be discussed in Chapter 6. Concluding remarks will be given in Chapter 7.

2. A CATHETER TRACKING METHOD USING REVERSED POLARIZATION FOR MR-GUIDED INTERVENTIONS

2.1 Introduction

The MRI is a very promising option for accurate guidance of complicated interventional procedures and provides high soft tissue contrast, but visualization of interventional devices is rather difficult. With this aim, many tracking techniques have been developed. Automatic identification of the position of the catheter in passive tracking techniques (5) is difficult. On the other hand, in active catheter tracking techniques (4,18), it is possible to obtain a catheter and background image simultaneously. However, the catheters need to be electrically connected to the scanner and this may cause RF safety problems and causes difficulties in device handling. Recently, Quick *et. al.* proposed wireless active catheter visualization (7) by using an inductively coupled RF (ICRF) coil; this can be classified as an intermediate method between active and passive techniques. The design is a good compromise that reduces the heating problems and simplifies the device handling. However, as in the passive tracking techniques, catheter and background images are not obtained simultaneously. Furthermore, wireless tracking method does not give satisfactory results for all flip angles. When larger flip angles are used, a poor contrast between ICRF coil and background is obtained.

In our study, we propose a novel technique for catheter tracking using an ICRF coil that enables simultaneous acquisition of background and catheter images separately thus allowing real-time, color-coded display (24,25) of the ICRF coil on background image, therefore drastically increasing accuracy of catheter tracking in an MRI scanner. In this technique, the reverse polarization mode is used to obtain an image of the ICRF coil; the forward polarization mode is used to obtain body image. Here we show that simultaneous acquisition of signals using both reverse and forward polarization modes is possible using a specially designed receive-only birdcage coil. We also demonstrate the feasibility of the proposed method with an in-vivo animal experiment.

2.2 Theory

In this section, we explain the relation between an ICRF coil and polarization of a signal.

2.2.1 Polarization of Received MRI Signal

Received MRI signal is proportional to the sensitivity of receiver radio frequency (RF) coil and the sensitivity of a coil can be formulated by the reciprocity principle as the circular polarized component of the magnetic field generated by the coil at the point of interest when a unit current is applied to the terminal of the coil. Circular polarization can be in forward or in reverse directions. Direction of a forward polarized field is the direction pointed by our right-hand fingers when thumb points to main magnetic field. Assuming that main magnetic field is in the positive z-direction, , forward polarized field can be written using the phasor notation (21) as:

$$H_f = \left(H_x - i\,H_y\right)/\sqrt{2}$$

where H_x and H_y are complex magnetic field components in the ***x*** and ***y*** directions respectively and $i=\sqrt{-1}$. On the other hand, we represent reverse polarized field using phasor notation by $H_r = \left(H_x + iH_y\right)/\sqrt{2}$. Transverse component of RF magnetic field, $\overrightarrow{H}$, can be written as the sum of forward and reverse polarization fields as:

$$\overrightarrow{H} = H_f \cdot \hat{a}_f + H_r \cdot \hat{a}_r$$

where $\hat{a}_f$ and $\hat{a}_r$ are forward and reverse magnetic field unit vectors and they can be written in terms of Cartesian coordinate unit vectors as $\hat{a}_f = \left(\hat{a}_x + i\hat{a}_y\right)/\sqrt{2}$ and $\hat{a}_r = \left(\hat{a}_x - i\hat{a}_y\right)/\sqrt{2}$.

In MRI, spins are excited by the reverse polarized component of the magnetic field and the signal is received by the forward polarized component of the magnetic field generated by an RF coil (26).

2.2.2 Standard Birdcage Coil

Standard birdcage (8) coil is used widely since it is first introduced in 1985 by Hayes *et. al.* There are two main advantages of the birdcage coil: first, it creates homogenous magnetic field; second; it can be built as quadrature coil easily. Standard quadrature birdcage coils are design to be sensitive to circularly polarized magnetic field. This is done by the help of a quadrature hybrid circuit. In order to explain this effect, we again use reciprocity. A unit current applied to one of the two feeds of the birdcage coil generates uniform magnetic field in ***x***-direction suggesting that signal received from this feed is the ***x***-component of the magnetization vector. Similarly, when the other feed is used to receive MRI signal, it becomes sensitive to ***y***-component of the magnetization vector. If the signal received from feed 2 (***y***-channel) is 90^0 phase delayed before adding to the other, a coil sensitive to forward component of the polarization is obtained. In phasor notation this phase delay can be represented by multiplying by complex number $-i$. (Figure 2.1).

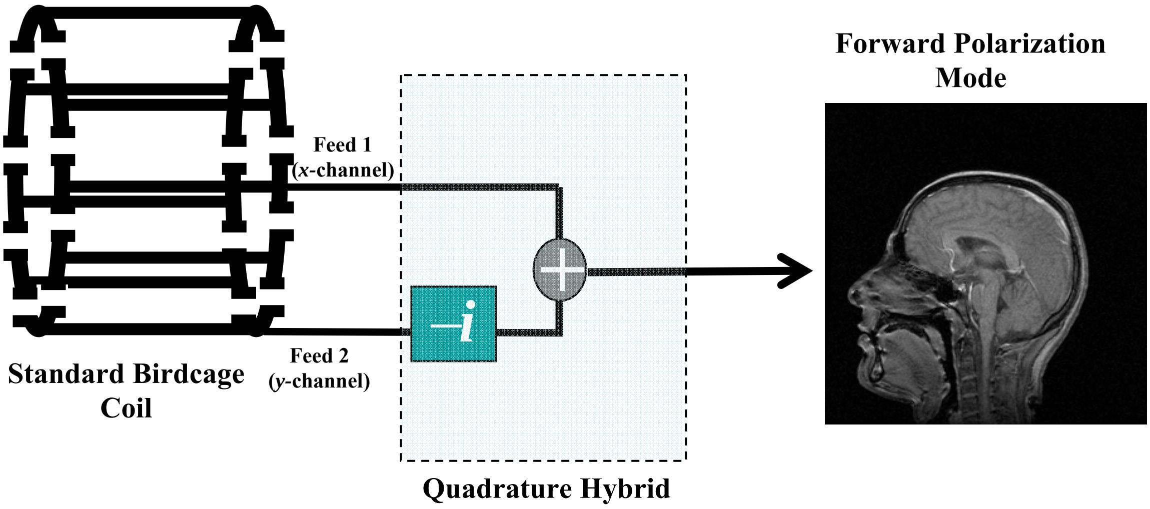

Figure 2.1: Standard birdcage coil configuration. The birdcage coil has two feeds and they are connected to a quadrature hybrid. The quadrature hybrid creates a 90^0 phase difference between ***x*** and ***y*** components of the received signals and adds to obtain the forward polarization mode signal.

On the other hand, if we connect feeds of the birdcage coil in reverse order, the signal received from feed 2 (***y***-channel) is 90^0 phase-advanced before adding to the other, this time, the coil becomes sensitive to reverse component of the polarization. In phasor notation this phase delay can be represented by multiplying by complex number $+i$. Ideally, resultant image should consist of only noise. However, because of imperfections in birdcage coil and quadrature hybrid designs we receive some signals (Figure 2.2), but reconstructed image becomes very noisy.

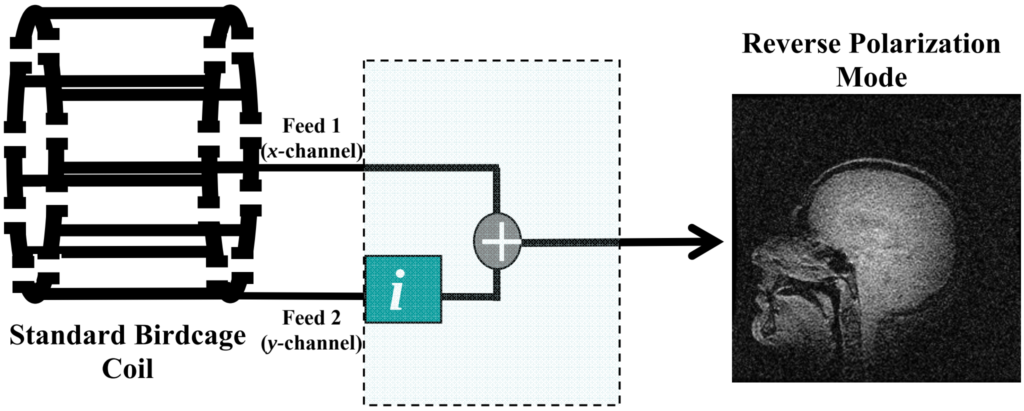

Figure 2.2: Reverse polarization mode image of standard birdcage coil. In perfect systems, if the phase of the MRI signal from feed 2 (***y***-channel) is advanced by 90^0 before adding, no MRI signal can be detected. The same effect can be obtained by cross connecting the feeds to the quadrature hybrid connections. However, imperfect systems may result in some signals as seen in the figure.

2.2.3 Implementing Quadrature Hybrid Using Computer Programs

Phase manipulation can also be done using software. If we multiply image raw data by a constant $\boldsymbol{i}$ or $\boldsymbol{e}^{i\pi/2}$, the magnitude of the pixel value will remain unchanged but its phase will increase by $\pi/2$. Addition operation is also very straightforward for a computer program therefore if the signals from feeds 1 and 2 are directly acquired, the function of the quadrature hybrid can be imitated by a simple computer program.

2.2.4 Linear Polarization

ICRF coils have typically very simple structures and therefore they work in linear polarization mode. By this property ICRF coils change the polarization of the MR signal by receiving forward polarized MRI signal from the body and retransmits it to the receiver coil in the form of a linearly polarized signal. Note that, a linearly polarized signal can be decomposed into forward and reverse polarized signals (Figure 2.3). Therefore if we design a coil that picks up only reverse polarized signal, the signal originated from the ICRF coil will be received but no other MR signal that directly comes from body can be detected.

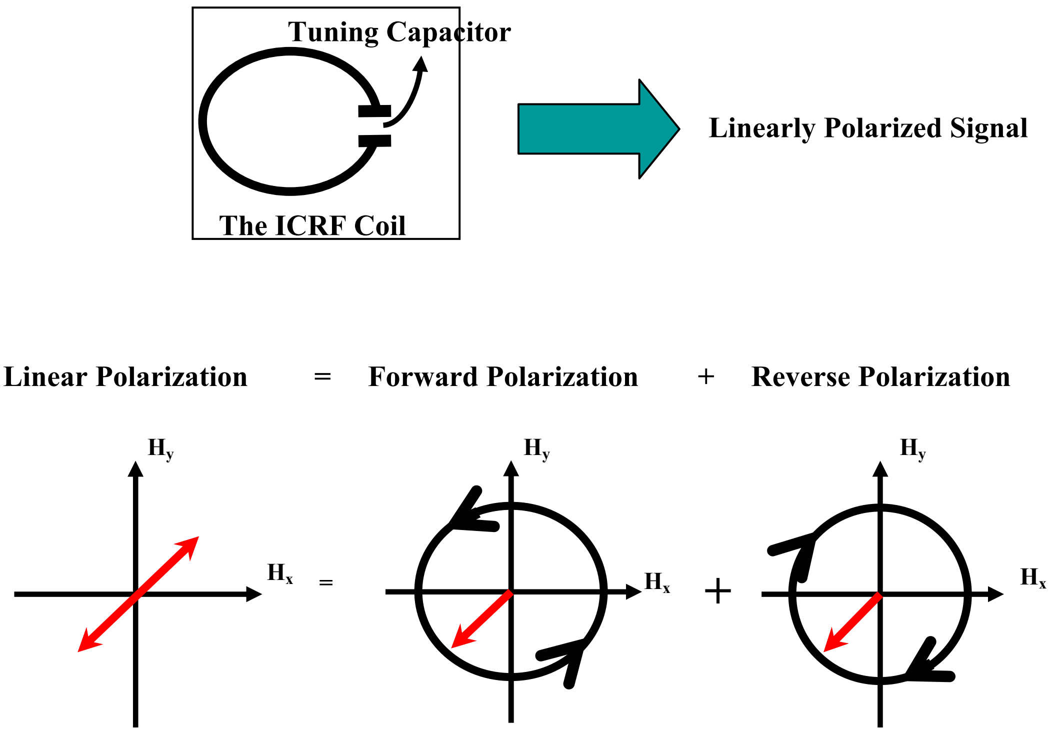

Figure 2.3: The inductively coupled RF (ICRF) coil and linear polarization. MR signal induces current on an ICRF coil and this creates a linear polarized signal. A linearly polarized signal can be decomposed into forward and reverse polarized signals. Therefore, an ICRF coil functions as a polarization converter.

2.3 Method

2.3.1 Receive-Only Birdcage Coil

We built a conventional receive-only birdcage coil with 12 legs but without a quadrature hybrid circuit. Two diodes for two feeds are used for decoupling using DC current comes from imager. Additionally, two pairs of back-to-back diodes are used for passive decoupling (See Figure 2.4).

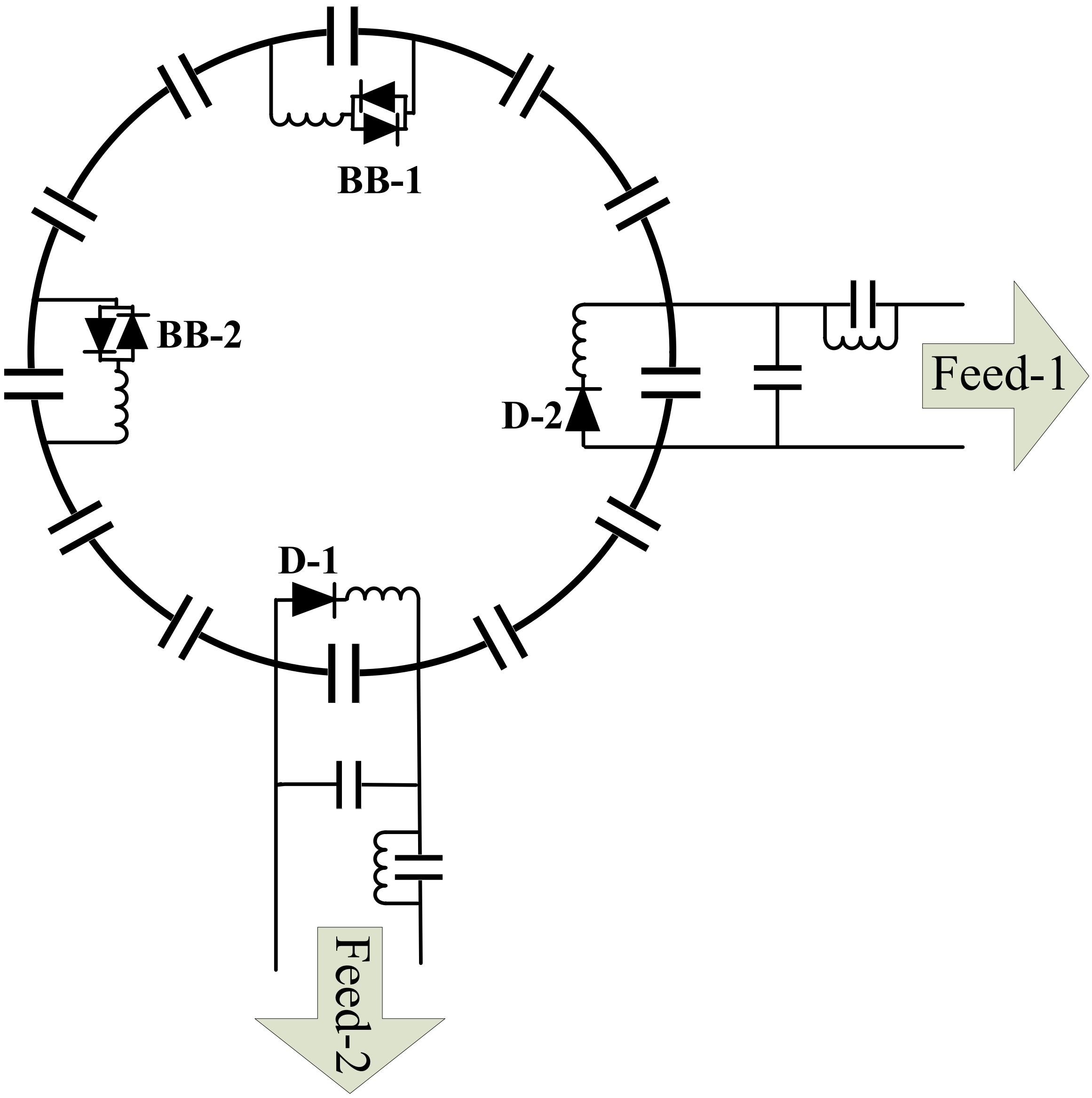

Figure 2.4: Sketch of the upper end-ring part of the receive-only birdcage coil. The receive-only birdcage coil has two feeds and inductor-diode system (D-1 and D-2) is used for decoupling. Scanner supplied DC current turns on the diode during RF transmission. In addition, two back-to-back diodes (BB-1 and BB-2) are used for passive decoupling. Again, during the RF transmission, AC current on the end-ring turns on BB-1 and BB-2 diodes which detune the coil resulting an effective decoupling.

When the imager transmits power, DC current turns on diodes D-1 and D-2 and resonance frequency shifts. In order to achieve better decoupling, two pairs of back-to-back diodes are connected to opposite capacitors of feeds are placed as shown in Figure 2.4. Back-to-back diodes are turned on as a result of AC current on end-ring. The combination of this active and passive decoupling techniques results in an effective decoupling. In this design two feeds of the coil are not fed into a quadrature hybrid instead it is directly connected to the dual phased array connector of a 1.5 T GE Signa Excite MR scanner with the idea that the function of the quadrature hybrid can be carried out in a MATLAB (version 7.0; Mathworks Inc.) code.

2.3.2 Inductively Coupled RF Coil

Two types of ICRF coil are built. The first one is a single loop ICRF coil without back-to-back decoupling diodes, which has a diameter of 2.1 mm and length of 10 cm. It is constructed from 0.4 mm diameter coated copper wire (see Figure 2.5). The coil is tuned by a ceramic chip capacitor (ATC Ceramics) to 63.85 MHz using an HP 8753D network analyzer.

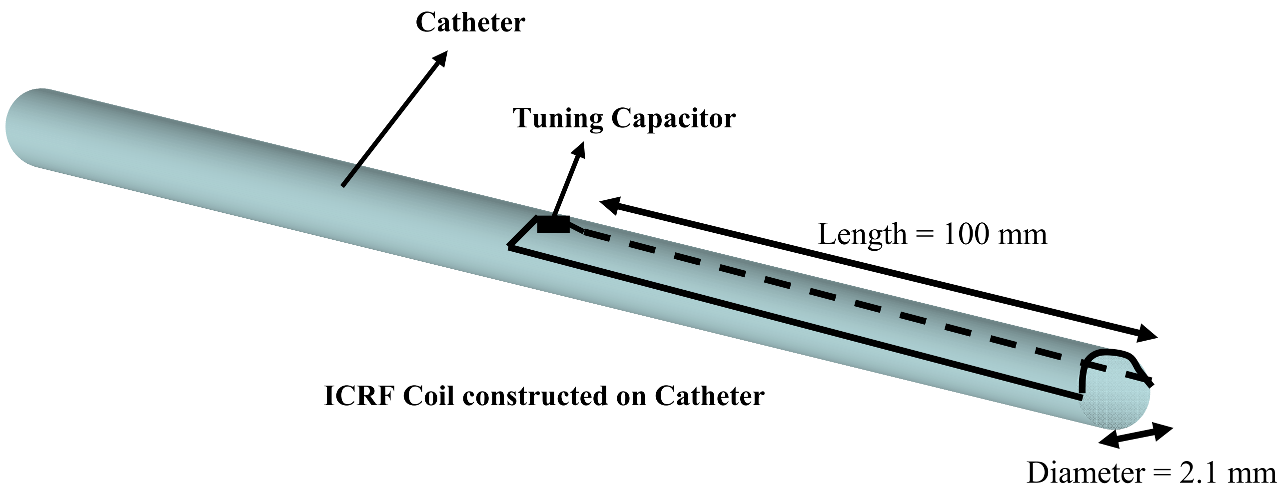

Figure 2.5: The ICRF coil without decoupling. The ICRF coil has a diameter of 2.1 mm and length of 10 cm. It is constructed from 0.4 mm diameter coated copper wire. The ICRF coil is tuned by a ceramic chip capacitor to 63.85 MHz using an HP 8753D network analyzer.

The second type ICRF coil has the same construction except that a pair of back-to-back diodes in parallel to the tuning capacitor is added. Similar to passive decoupling in the receive-only birdcage coil, diodes are turned on when RF signal is applied. This eventually reduces the induced RF current on the ICRF coil and therefore image artifacts are reduced.

2.3.3 Phantom Experiment

In our phantom experiments, gel filled bottles were used. Images acquired using fast gradient echo using the following imaging protocol: TR/TE: 40/3.4 ms, flip angle: 40^0, slice thickness: 5 mm, spacing: 1 mm, matrix: 256 X 256, FOV: 300 X 300 mm^2.

2.3.4 Animal Experiment

Proof of principle experiments were conducted using the ICRF coil without decoupling diodes. The ICRF coil was constructed on a naso-gastric tube. Experiments had been conducted in conformity with the Guidelines for the Care and Use of Laboratory Animals, and were approved by Gazi University ethics committee, Ankara, Turkey. Imaging was performed with a 1.5 T MR scanner (Signa; Excite, GE medical systems; Milwaukee, Wisconsin). One healthy New Zealand rabbit was used in our study. General anesthesia was induced by intramuscular injection of 5 mg/kg of ketamine and 40 mg/kg of xylazine. Following general anesthesia, the ICRF coil was lubricated and inserted orally to duodenum. The rabbit was then placed on an MR couch and imaging was performed while the coil is moved out through the esophagus. The motion of the tube inside the esophagus of a rabbit was recorded by acquiring fast gradient echo images using the following imaging protocol: TR/TE: 10/1.5 ms, flip angle: 40^0, slice thickness: 5 mm, matrix: 256 X 256, FOV: 256 X 160 mm^2.

2.3.5 Visualization of the ICRF Coil

Spins produce a forward polarized signal in the receive-only birdcage coil (See Figure 2.6). When we place the ICRF coil inside the coil, spin rotation induces a current on the ICRF coil. This current also produces a signal, which is linearly polarized. As explained in theory section, linearly polarized signal consists of both forward and reverse polarized signals. With the above mentioned experiments we obtained two signals; one corresponding to the sensitivity in the ***x***-direction and the other corresponding to the ***y***-direction. Both of these signals were uploaded to a laptop for post-processing. By adding received signals from ***x*** and ***y***-channels after multiplying ***y***-channel signal by ***-i***, forward polarized mode signal is reconstructed. On the other hand, multiplying ***y***-component by ***i*** reverse polarized mode signal was generated. After these manipulations, the images were obtained by using standard 2D-FFT computation.

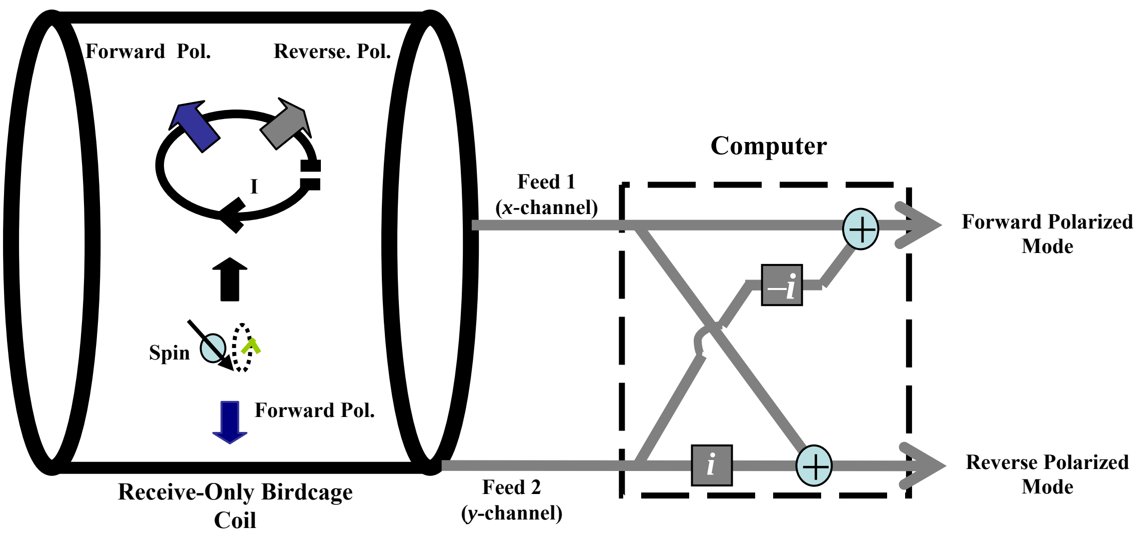

Figure 2.6: Visualization process of the ICRF coil and the body. Spins in the body creates a forward polarized signal. If an ICRF coil is placed in the RO birdcage coil, spin rotation induces current on the ICRF coil and it creates linear polarized signal, which consists of both forward and reverse polarized signals. By feeding ***x*** and ***y***-channels directly to the scanner, both forward and reverse polarized modes can be reconstructed.

As a result we reconstructed two images representing forward and reverse polarized modes. In the forward polarized image, conventional image of the body with the ICRF coil was reconstructed. On the other hand, reverse polarized mode resulted in only the ICRF coil image

2.4 Results

2.4.1 Phantom Experiment

Two different ICRF coil are used in phantom experiment. In Figure 2.7, the ICRF coil without decoupling diodes images are seen. Image of the ICRF coil shows some artifacts (Figure 2.7a), because of a strong coupling of ICRF during RF transmit.

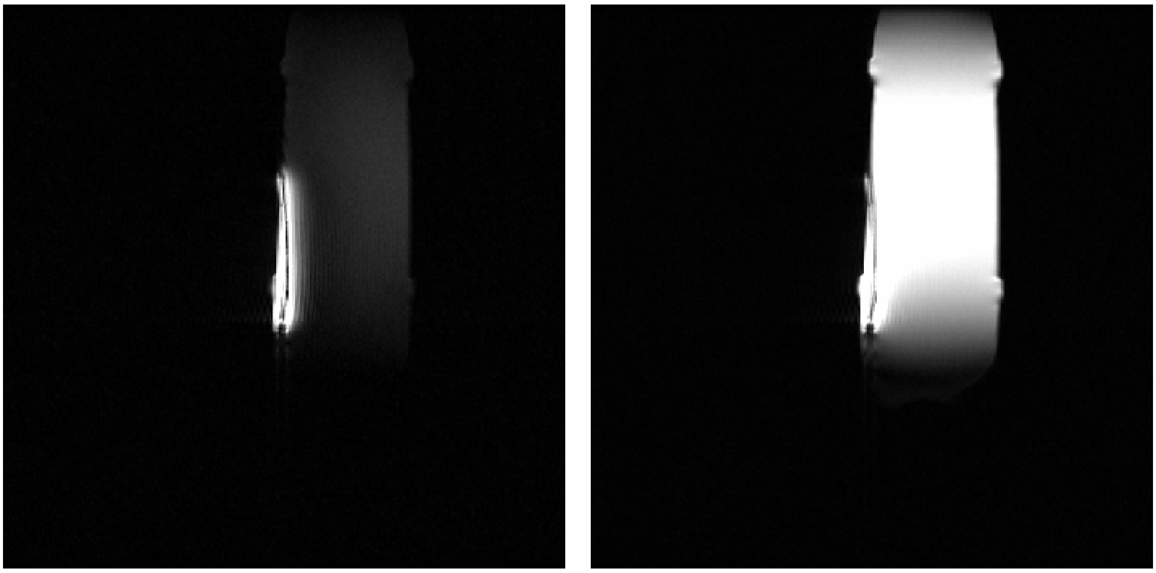

a) b)

Figure 2.7: Phantom experiment of the ICRF coil without decoupling diodes. **a)** Reverse polarization mode image. Note that, because of strong decoupling, the image ICRF coil is disturbed. **b)** Forward polarization mode image.

On the other hand, back-to-back diodes at ICRF result in decoupling artifact free images. Hence, the quality of the ICRF coil images is improved (See Figure 2.8).

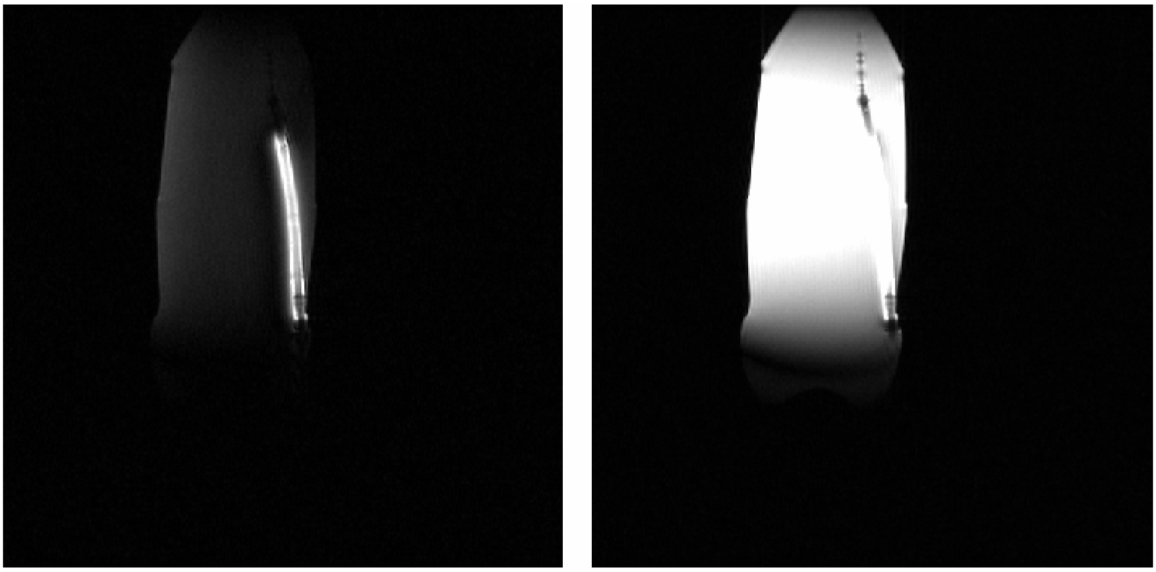

Figure 2.8: Phantom experiment of ICRF coil with decoupling diodes. **a)** Reverse polarization mode image. **b)** Forward polarization mode image. As seen in Figure 2.8a, decoupling diodes increases visibility of the ICRF coil.

2.4.2 Animal Experiment

In order to show the effectiveness of the new method, we acquired inductively coupled images using a SSFP sequence with 40^0 flip angle. The ICRF coil without decoupling diodes is used in animal experiment. As Figure 2.9a shows, it is difficult to see where the catheter is if a standard image reconstruction technique is used. By using a reverse polarization mode, we are able to eliminate background from the catheter image (See Figure 2.9b) and overlay the color-coded catheter image on the background (See Figure 2.9c).

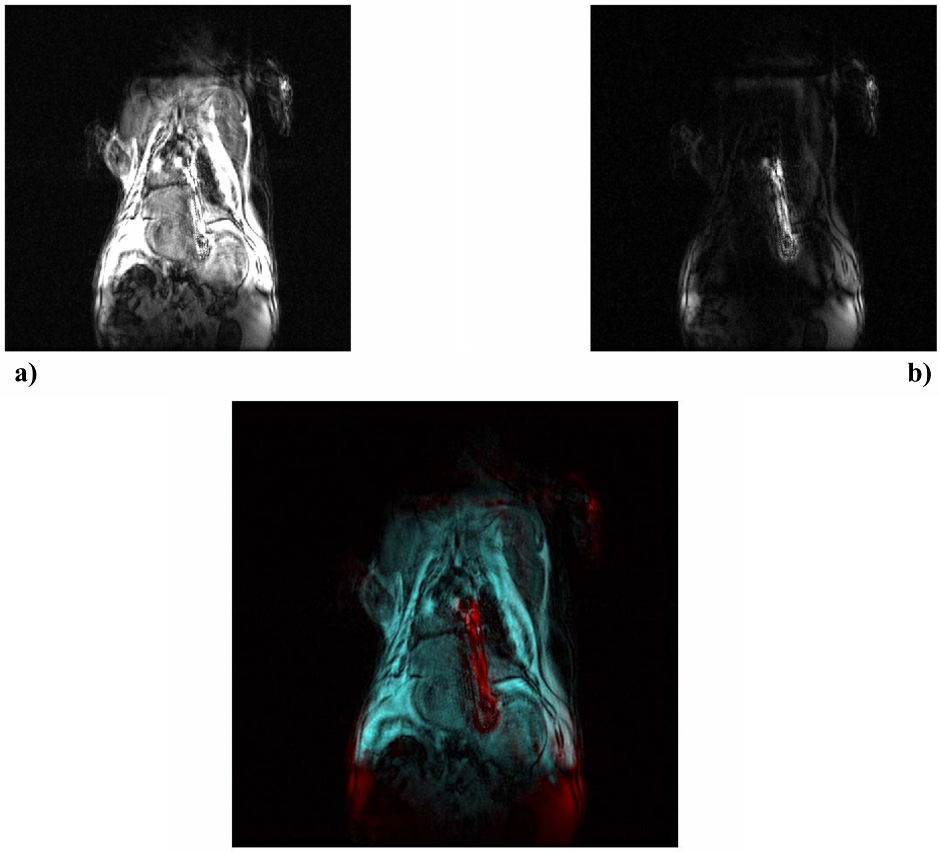

a) b)

c)

Figure 2.9: Rabbit experiment results. We placed a modified naso-gastric tube inside the esophagus of the animal. **a)** Forward polarization mode image. It is difficult to distinguish the ICRF coil from the background. **b)** Reverse polarization mode image. In this mode, ICRF coil clearly visible and background signal is reduced. **c)** The forward and reverse polarized images are combined using color-coding.

2.5 Conclusion

A novel method of displaying both an inductively coupled coil and background body image on a color-coded image has been demonstrated. We have tested the effectiveness of this method by phantom and animal experiments; however, usefulness of this technique needs to be tested in clinical practice.

3. WIRELESS ACTIVE CATHETER TRACKING METHOD USING REVERSED POLARIZATION OF PHASED ARRAY COILS FOR MR-GUIDED INTERVENTIONS

3.1 Introduction

Accurate visualization of guidewires and catheters during a vascular intervention (4,18) procedure is critically important. With this aim, many tracking techniques have been developed. Automatic identification of the position of the catheter in passive tracking techniques (5) is difficult, while in active catheter tracking techniques (4,7,18), it is possible to obtain a catheter and background image simultaneously. In active techniques, however, the catheters need to be electrically connected to the scanner and this potentially causes both RF safety problems and creates difficulties in device handling. Recently, Quick et.al. proposed wireless active catheter visualization (7) by using an inductively coupled RF (ICRF) coil. This can be classified as an hybrid method of active and passive techniques. The wireless catheter design enables reduction of RF heating problems and simultaneously improves device handling. The inductively coupled catheter coils locally amplify the RF excitation flip angle and thus the signal around the vascular instruments, enabling visualization of the instruments with high signal in real-time MR images. While the instrument as well as the blood provide bright signal in TrueFISP images, the instrument to background contrast, however, might be limited rendering it hard to depict the instrument from the background signal.

Earlier we have proposed a method of obtaining ICRF coil-only images. However, this method required the use of a specially designed birdcage coil, which can acquire forward and reverse polarization mode data simultaneously (27). However, this birdcage coils are not optimal in many imaging procedures.

In the present study, we propose a novel technique for catheter tracking of inductively coupled RF coil that enables simultaneous acquisition of background and catheter images with, color-coded display of the RF coil on the background image from any phased array coil image. In this technique, the raw phased array coil data was processed to obtain reverse and forward circular polarization mode information. Reverse circular polarization is used to generate ICRF coil image, whereas forward polarization mode was used to generate background image.

3.2 Theory

In this section, we explain the relation between an ICRF coil and polarization of a signal.

3.2.1 Polarization of Received MRI Signal

Received MRI signal is proportional to the sensitivity of receiver radio frequency (RF) coil and the sensitivity of a coil can be formulated by the reciprocity principle as the circular polarized component of the magnetic field generated by the coil at the point of interest when a unit current is applied to the terminal of the coil. Circular polarization can be in forward or in reverse directions. Direction of a forward polarized field is the direction pointed by our right-hand fingers when thumb points to main magnetic field. Assuming that main magnetic field is in the positive z-direction, , forward polarized field can be written using the phasor notation (21) as:

$$H_f = \left(H_x - i\,H_y\right)/\sqrt{2} \qquad [1]$$

where H_x and H_y are complex magnetic field components in the $\boldsymbol{x}$ and $\boldsymbol{y}$ directions respectively and $i = \sqrt{-1}$. On the other hand, we represent reverse polarized field using phasor notation by $H_r = \left(H_x + iH_y\right)/\sqrt{2}$. Transverse component of RF magnetic field, $\overrightarrow{H}$, can be written as the sum of forward and reverse polarization fields as:

$$\overrightarrow{H} = H_f \cdot \hat{a}_f + H_r \cdot \hat{a}_r \qquad [2]$$

where $\hat{a}_f$ and $\hat{a}_r$ are forward and reverse magnetic field unit vectors and they can be written in terms of Cartesian coordinate unit vectors as $\hat{a}_f = \left(\hat{a}_x + i\hat{a}_y\right)/\sqrt{2}$ and $\hat{a}_r = \left(\hat{a}_x - i\hat{a}_y\right)/\sqrt{2}$.

In MRI, spins are excited by the reverse polarized component of the magnetic field and the signal is received by the forward polarized component of the magnetic field generated by an RF coil (26).

3.2.2 Linear Polarization

ICRF coils have typically very simple structures and therefore they work in linear polarization mode. By this property ICRF coils change the polarization of the MR signal by receiving forward polarized MRI signal from the body and retransmits it to the receiver coil in the form of a linearly polarized signal. Note that, a linearly polarized signal can be decomposed into forward and reverse polarized signals (Figure 3). Therefore if we design a coil that picks up only reverse polarized signal, the signal originated from the ICRF coil will be received but no other MR signal that directly comes from body can be detected.

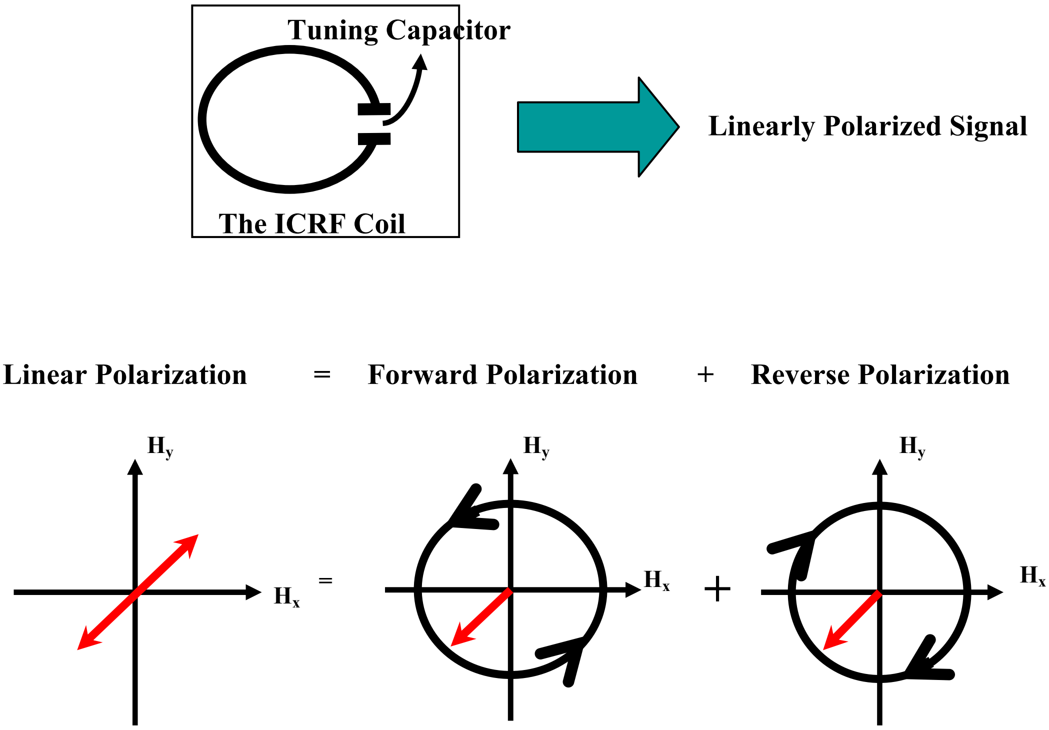

Figure 3.1: The inductively coupled RF (ICRF) coil and linear polarization. MR signal induces current on an ICRF coil and this creates a linear polarized signal. A linearly polarized signal can be decomposed into forward and reverse polarized signals. Therefore, an ICRF coil functions as a polarization converter.

3.2.3. Phased Array Coils

Assume we have N-channels phased array coil and each individual coil has magnetic field of

$$\overline{H}_n = \left(H_{nx}\hat{a}_x + jH_{ny}\hat{a}_y\right) \qquad [3]$$

where n is channel (coil, slice) number and n=1,2,…,N. Sensitivity is proportional to this field, then if we ignore phase differences, we can express sensitivity as

$$S_n = \omega\mu\overline{H}_n \qquad [4]$$

where ω is Larmour frequency, μ is magnetic permittivity, and $\hat{a}_r = \left(\hat{a}_x - i\hat{a}_y\right)/\sqrt{2}$ is reverse magnetic field unit vector. Now, assume we have an image of body without ICRF coil. Then, we know that the signal is received by the forward polarized component of the magnetic field generated by an RF coil. If the signal is a reverse polarization mode of image, coil receives no signal. Field created by a coil which receives with the reverse mode can be expressed as:

$$H_r = H_0\left(\hat{a}_x - j\hat{a}_y\right) \qquad [5]$$

Resultant signal is

$$S_i = M_0\hat{a}_r \cdot S_n \qquad (0.6)$$

where S_n is sensitivity and M_0 is magnetization. Resultant signal becomes zero:

$$S_i = M_0\hat{a}_r \cdot \left(\hat{a}_x - j\hat{a}_y\right)\omega\mu H_0 = 0 \qquad (0.7)$$

Assume we acquire signals using *N*-channels phased array coil to form an image of 512 X 256. We obtain a matrix of 512 X 256 X *N*, where each pixel consists of real and imaginary components and there are *N*-different complex numbers that contribute to a pixel on the resultant image.

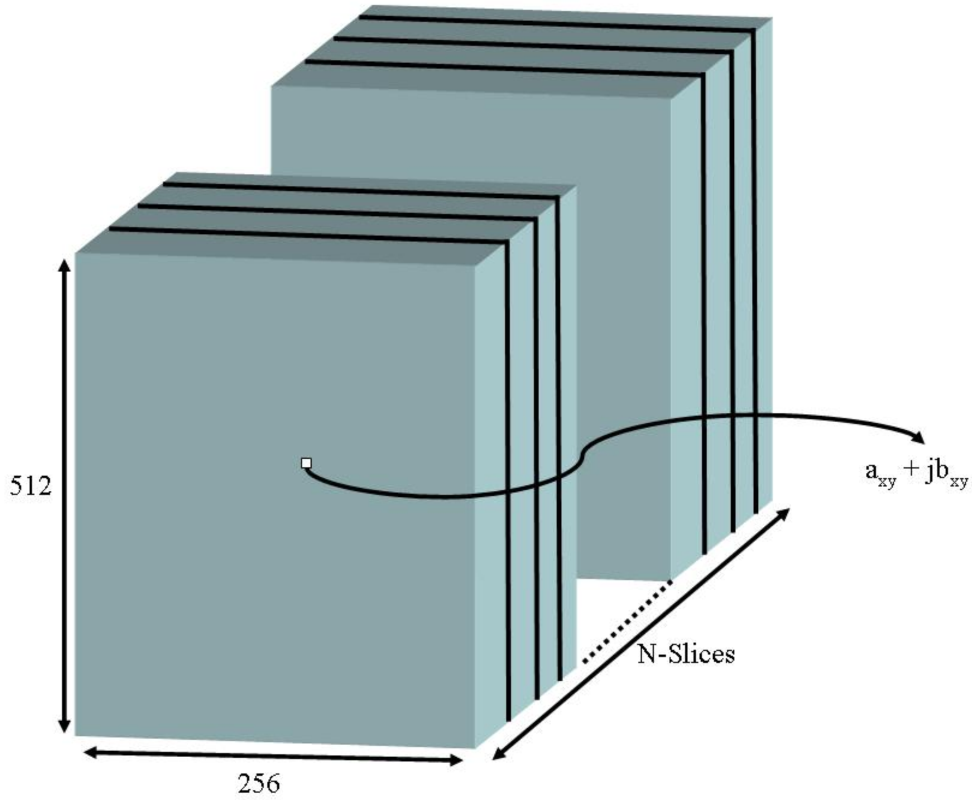

Figure 3.2: Schematic representation of acquired image data. Images are 512 X 256 and there are *N* images from *N* channels.

If we take square of *N* pixels, sum them up, and repeat this for all 512 X 256 pixels, we obtain one 512 X 256 pixels image. If we multiply each pixel with an appropriate complex constant to reconstruct reverse polarization mode image, signal becomes zero:

$$\sum_{n=1}^{N} c_n \overline{H}_n = H_0 \left(\hat{a}_x - j\hat{a}_y \right) \text{ and } S_i = M_0 \omega \mu H_0 \left(\hat{a}_r \cdot \hat{a}_r \right) = 0 \qquad [8]$$

where c_n is n^{th} complex constant, H_0 is a constant. We can form a matrix equation for each pixel

$$\begin{bmatrix} H_{1x} & \cdots & H_{Nx} \\ H_{1y} & \cdots & H_{Ny} \end{bmatrix} \cdot \begin{pmatrix} c_1 \\ \vdots \\ c_N \end{pmatrix} = H_0 \begin{bmatrix} 1 \\ -j \end{bmatrix} \qquad [9]$$

As a result, we obtain N constants for N channel by using pseudo-inverse technique

$$\bar{c} = H_0 \left(\overline{\overline{H}}^T \cdot \overline{\overline{H}} \right)^{-1} \overline{\overline{H}}^T \begin{bmatrix} 1 \\ -j \end{bmatrix} \qquad [10]$$

If we make all calculations, we obtain c

$$\begin{pmatrix} c_1 \\ \vdots \\ c_N \end{pmatrix} = \frac{1}{D} \begin{bmatrix} AH_{1y} + CH_{1x} - j\left(AH_{1x} + BH_{1y} \right) \\ AH_{2y} + CH_{2x} - j\left(AH_{2x} + BH_{2y} \right) \\ \vdots \\ AH_{Ny} + CH_{Nx} - j\left(AH_{Nx} + BH_{Ny} \right) \end{bmatrix} \qquad [11]$$

where

$A = -\left(H_{1x}H_{1y} + H_{2x}H_{2y} + \ldots + H_{Nx}H_{Ny} \right)$

$B = \left(H_{1x}^2 + H_{2x}^2 + \ldots + H_{Nx}^2 \right)$

$C = \left(H_{1y}^2 + H_{2y}^2 + \ldots + H_{Ny}^2 \right)$

$D = \left(H_{1x}^2 + H_{2x}^2 + \ldots + H_{Nx}^2 \right)\left(H_{1y}^2 + H_{2y}^2 + \ldots + H_{Ny}^2 \right) - \left(H_{1x}H_{1y} + H_{2x}H_{2y} + \ldots + H_{Nx}H_{Ny} \right)^2$

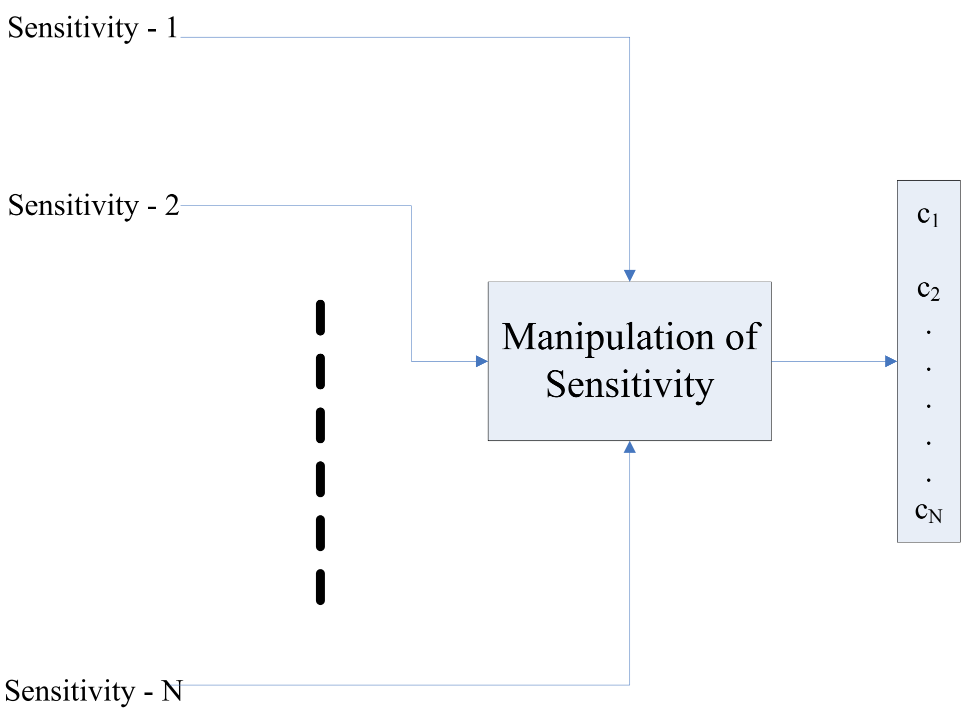

Figure 3.3: Flowchart for the case when there is only body image. Sensitivity is directly related to data come from channels.

Every pixel has a different constant *c*, so we obtain 512 X 256 X N constant values. If we multiply these complex constants with corresponding values, we obtain a zero filled image.

Above, we explained the case when we have only body. Now, assume we have both body and catheter. In this case, we cannot use *c* values directly, because, we now need to discriminate the sensitivity of the coil itself from the image of the catheter. In this case, ICRF coil manipulates the magnetization vector, $M_0\hat{a}_r$, to another form $QM_0\hat{a}_x$, where Q is voltage gain due to ICRF coil. Here, reverse magnetic field unit vector replaced by linearly polarized field unit vector $\hat{a}_x$. Because of this manipulation, resultant signal would not be equal to zero. Therefore, in order to obtain sensitivity information of the coil, we low-pass filter the data comes from each coils (1). Then we manipulate the data to form *c* vector.

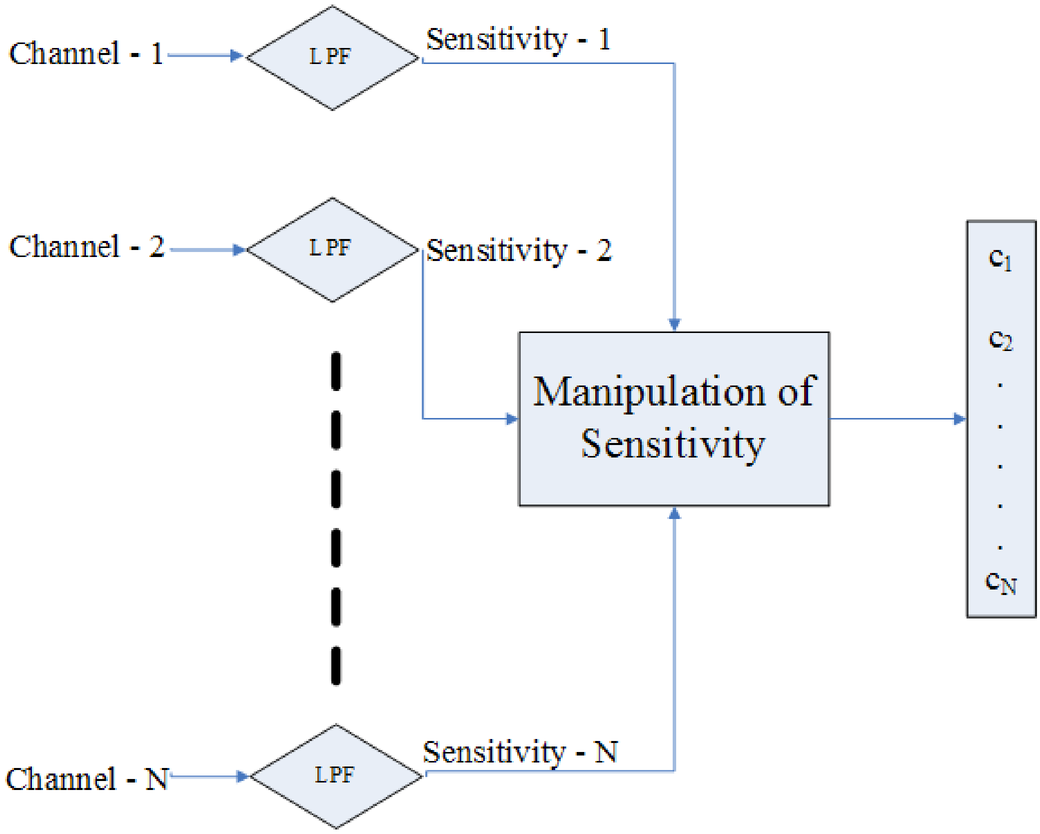

Figure 3.4: Flowchart for the case when there are both body and catheter images. In order to obtain *c* vector, low-pass filtering of the channel data are required before manipulations.

The manipulated data is approximate sensitivity of the coil and called *c* vector .Then, when we multiply *c* vector with appropriate channel data and sum all matrices, we obtain an image which consists of catheter only:

3.3 Method

In our work we used a 1.5 T Siemens Avanto imaging system and a 6-channels phased array coil. Each of the feeds is connected to the scanner directly using a phased array adaptor. This enabled us to reconstruct both forward and reverse polarization images with single acquisition. While the forward polarization images become the desired background image, the reverse polarization creates a background-free image of the inductively coupled coil.

Raw data files were obtained from six channels. In order to reconstruct the reverse polarized mode image, MATLAB (version 7.0; Mathworks Inc.) code was written. In the same program, forward polarization mode image was also obtained and the catheter and background images were combined to form a color coded image. For the experiment, a small inductively coupled RF loop implemented into a vascular catheter was introduced into a NaCl solution filled bottle phantom

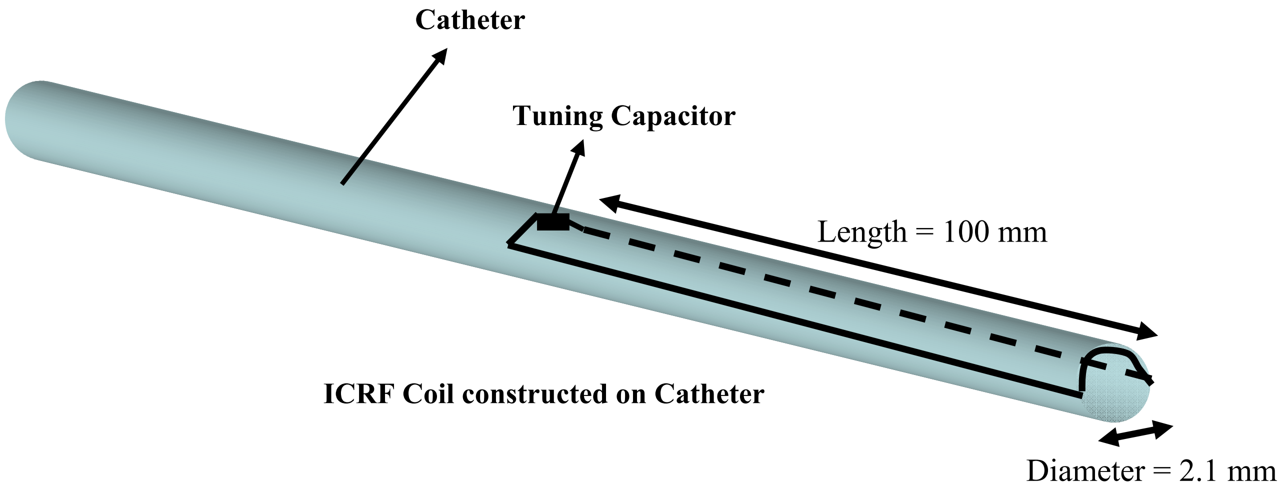

Figure 3.5: The ICRF coil without decoupling. The ICRF coil has a diameter of 2.1 mm and length of 10 cm. It is constructed from 0.4 mm diameter coated copper wire. The ICRF coil is tuned by a ceramic chip capacitor to 63.85 MHz using an HP 8753D network analyzer.

3.4 Results

In our phantom experiments, gel filled bottles were used. Images acquired using fast gradient echo using the following imaging protocol: TR/TE: 40/3.4 ms, flip angle: 40^0, slice thickness: 5 mm, spacing: 1 mm, matrix: 256 X 256, FOV: 300 X 300 mm^2.

Figure 1a shows a forward polarized mode image showing the catheter with the background. By using a reverse polarization image, we were able to eliminate background from the catheter image (see Figure 1b) and overlay the color-coded catheter image on the background (See Figure 1c.)

a) b) c)

Figure 3.6: **a)** Forward polarization mode image. **b)** Reverse polarized mode image. **c)** Color-coded image.

Below, flowchart of the method is shown for 6 channels phased array image. Matrix size is 512 X 256.

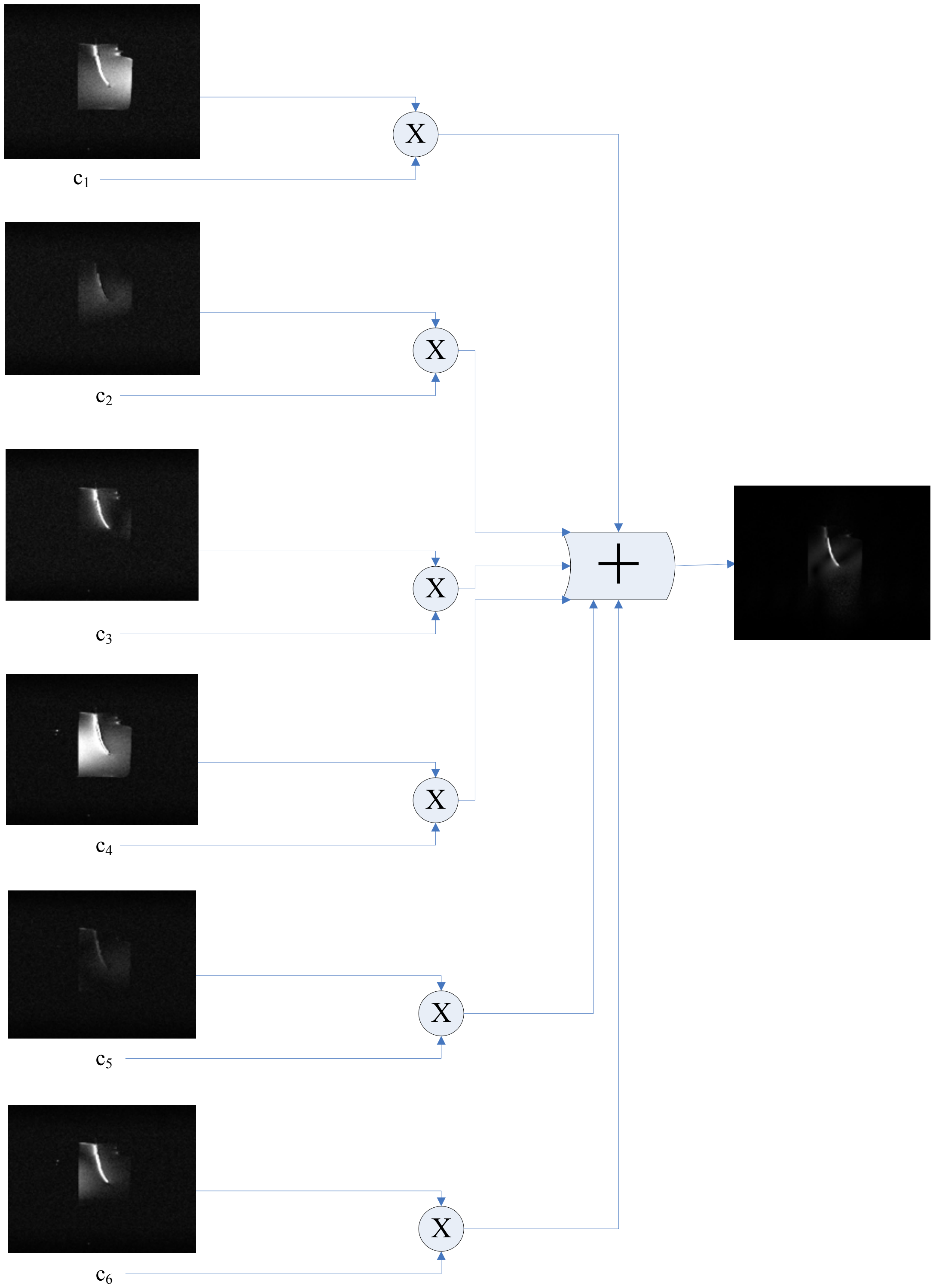

Figure 3.7: Flowchart for 6-channels phased array coil. In order to obtain reverser polarization mode of image, channel data is multiplied by a proper matrix and they are added up.

3.5 Conclusion

We have demonstrated a novel method for simultaneous acquisition of both inductively coupled coil and background images with the ability to color-code the instrument signal. This method can be used very effectively for accurate catheter tracking and for improved delineation of instrument to background signal when using wireless active catheter visualization.

4. AN INDUCTIVELY COUPLED RF (ICRF) COIL MARKER FOR BRAIN SURGERY

4.1 Preface

This project was done by a demand of IZI Medical Products, Baltimore. Kerim Kara helped to produce this chapter.

4.2 Introduction

During an invasive operation, targeting is critical. Especially, in brain surgery, fault targeting may cause severe results. Image guided surgery (IGS) is an effective method used in brain operation in order to increase reliability of the IGS. On the other hand, a link between the MR image and head of the patient arises; therefore, to register any lesions with the correct point on the body, some type of registration products introduced. Among others, Multi-Modality Markers (11) are most widely used registering products. However, in some sequences, these markers do not shine enough, so registering becomes harder.

In our study, we proposed an inductively coupled RF (ICRF) coil which increases signal intensity of Multi-Modality (Gel) Markers (MMM) for image guided surgery registration to make markers visible in all sequences.

4.3 Theory

There are various types of implantable coils (28) which are used in order to obtain better resolution. In Figure 4.1a, simple self-tuned inductively coupled RF coil is shown. Instead of using a capacitor for tuning, number of turns is adjusted so that coil resonates at Larmour frequency. Main problem with this configuration is low quality factor (Q). The lower quality factor the coil has, the lower signal intensity we obtain. In addition, there is no resonance blocking circuit (29) on the coil, so during transmit mode, current is induced on the coil and this current causes unwanted field which disturbs RF field generated by the coil. The second configuration is coil with a capacitor (See Figure 4.1b). This coil has higher Q factor and signal intensity as compared to the first design as expected. On the other hand, another design is self-resonated ICRF coil with decoupling circuit (See Figure 4.1c). Main difference of this design is undisturbed field near the coil. Although quality factor is small, similar to the first coil's case, we obtain better image quality. If we use only one diode for decoupling (See Figure 4.1d) we acquire better image than the first case, but it would not as good as the back-to-back diode design.

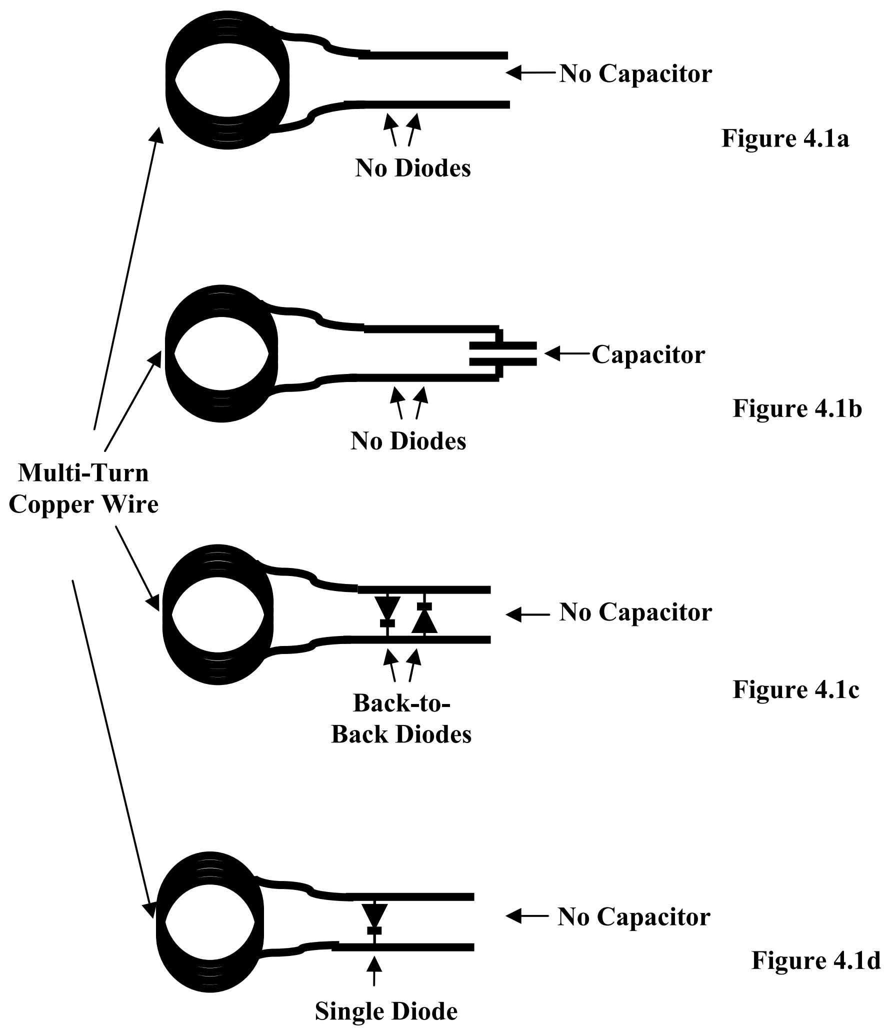

Figure 4.1: Different configurations of ICRF coils. **a)** Without capacitor and diode **b)** With tuning capacitor **c)** With decoupling diodes **d)** With single decoupling diode

In our project, we fabricated a coil with tuning capacitor and decoupling (8) back-to-back diodes (See Figure 4.2a). This design gives the best results among other imaging coils shown above. During transmission, passive decoupling circuit works and coil does not create any field. A current is induced on the ICRF coil and the field produced by the current is collected to reconstruct an image in reception mode.

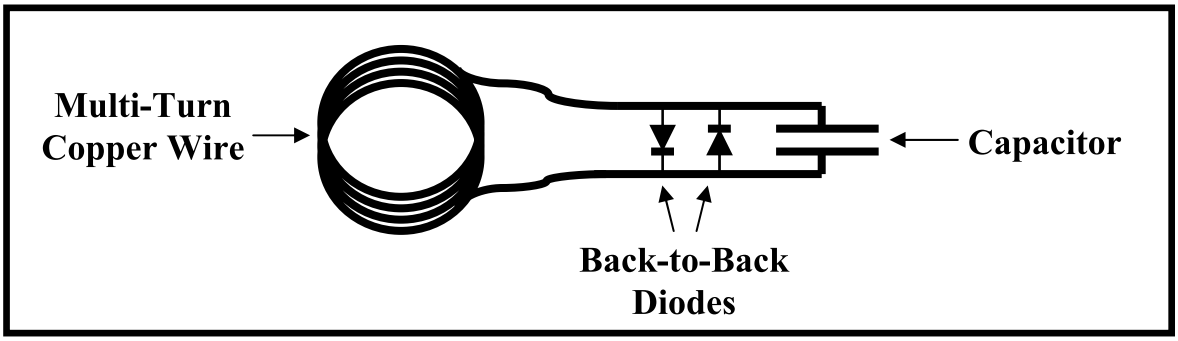

a) ICRF Coil with Decoupeler Circuit.

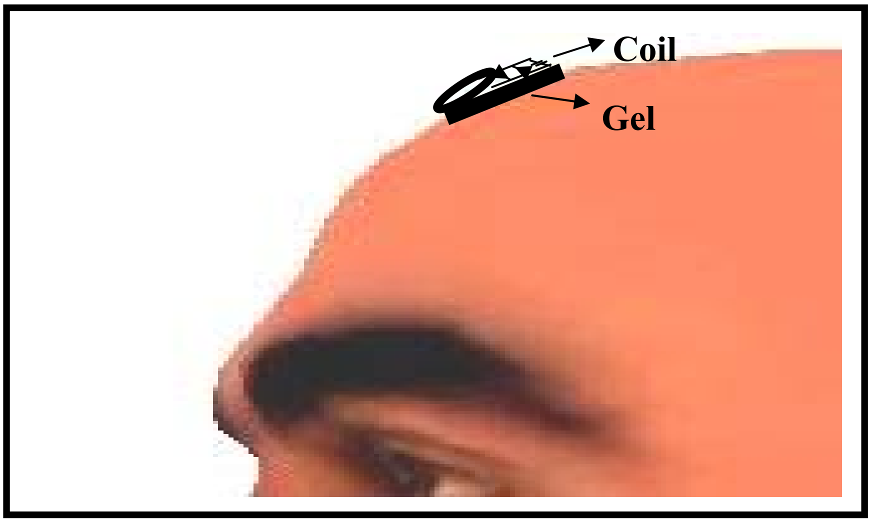

b) ICRF Coil and MM Marker are placed on forehead of the patient.

Figure 4.2: **a)** The ICRF coil with tuning capacitor and decoupling back-to-back diodes. **b)** Sketch of ICRF coil, MMM, and head of a patient.

Figure 4.3: Multi-Modality (Gel) Markers (IZI Medical Products). Zinreich introduced the gel for image-guided surgery and this marker is used with our ICRF coils.

4.4 Method

In our work we used a 1.5 T GE Signa Excite imaging system and two homemade ICRF coils with decoupling circuits. Diameters of the coils are 1.0 (Coil-1) and 1.5 (Coil-2) cm. Copper wire is used to fabricate coils and wire has 0.5 mm diameter. Smaller coil (Coil-1) is tuned with 34 pF and larger one (Coil-2) is tuned with 6.1 pF capacitors. Two back-to-back diodes are connected shunt to the capacitor as a decoupling circuit (See Figure 4.2a). ICRF coil and MMM is attached to forehead of a healthy person as seen Figure 4.2b.

4.5 Results

In order to show the effectiveness of the new method, we acquired three groups of images, the first one was Multi-Modality Marker without ICRF coil, the second was Coil-1 placed on top of Multi-Modality Marker, and the last one was Coil-2 placed on top of MMM.

In Figure 4.4a, image of the Multi-Modality Marker without an ICRF coil was shown. Coil-1 and Coil-2 with MMM images were shown in Figure 4.4b and Figure 4.4c respectively. For all images, same contrast parameters are used (W = 606, L = 333). Imaging parameters are TR/TE = 100/3000 msec, FOV = 240 mm, matrix = 512 X 256, slice thickness = 5 mm, spacing = 1.5 mm, echo train length = 16, and NEX = 1.

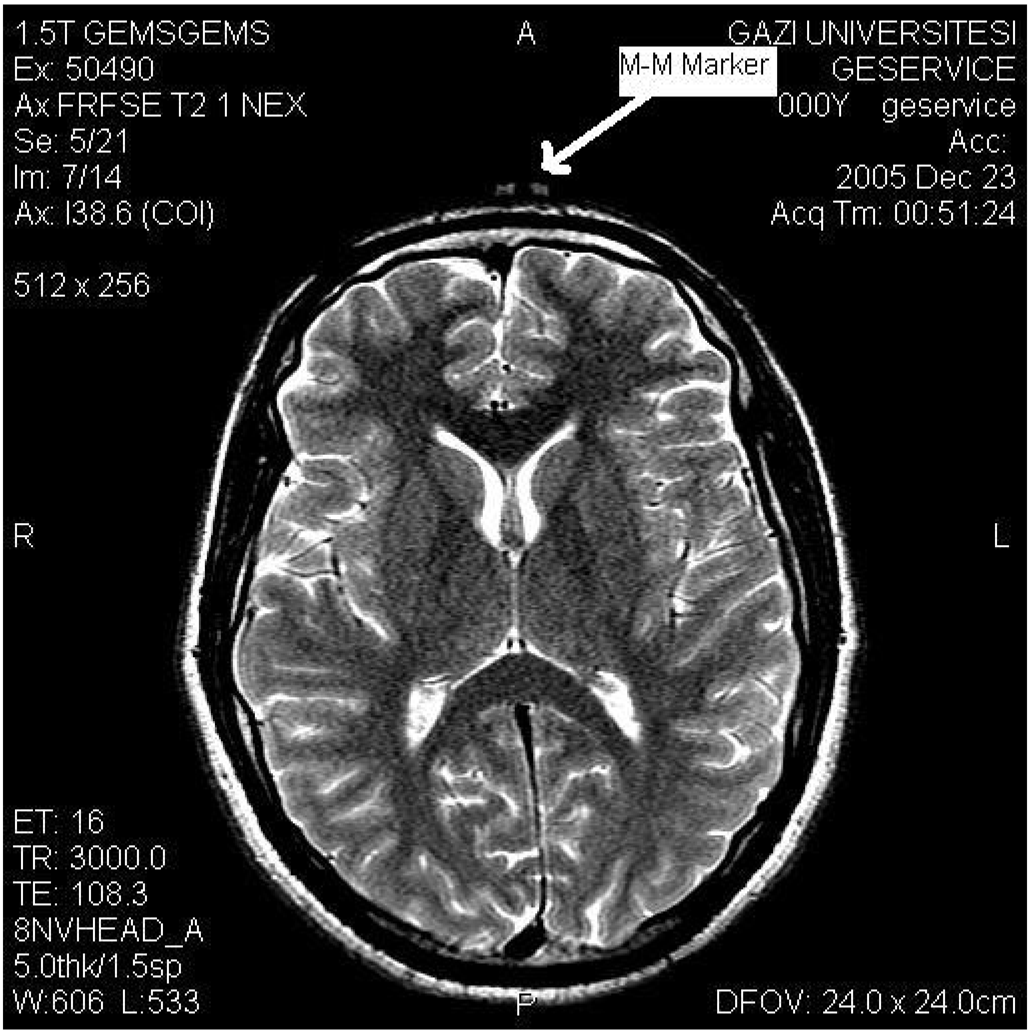

Figure 4.4: Multi-Modality Marker. As seen in the figure, marker is not clear.

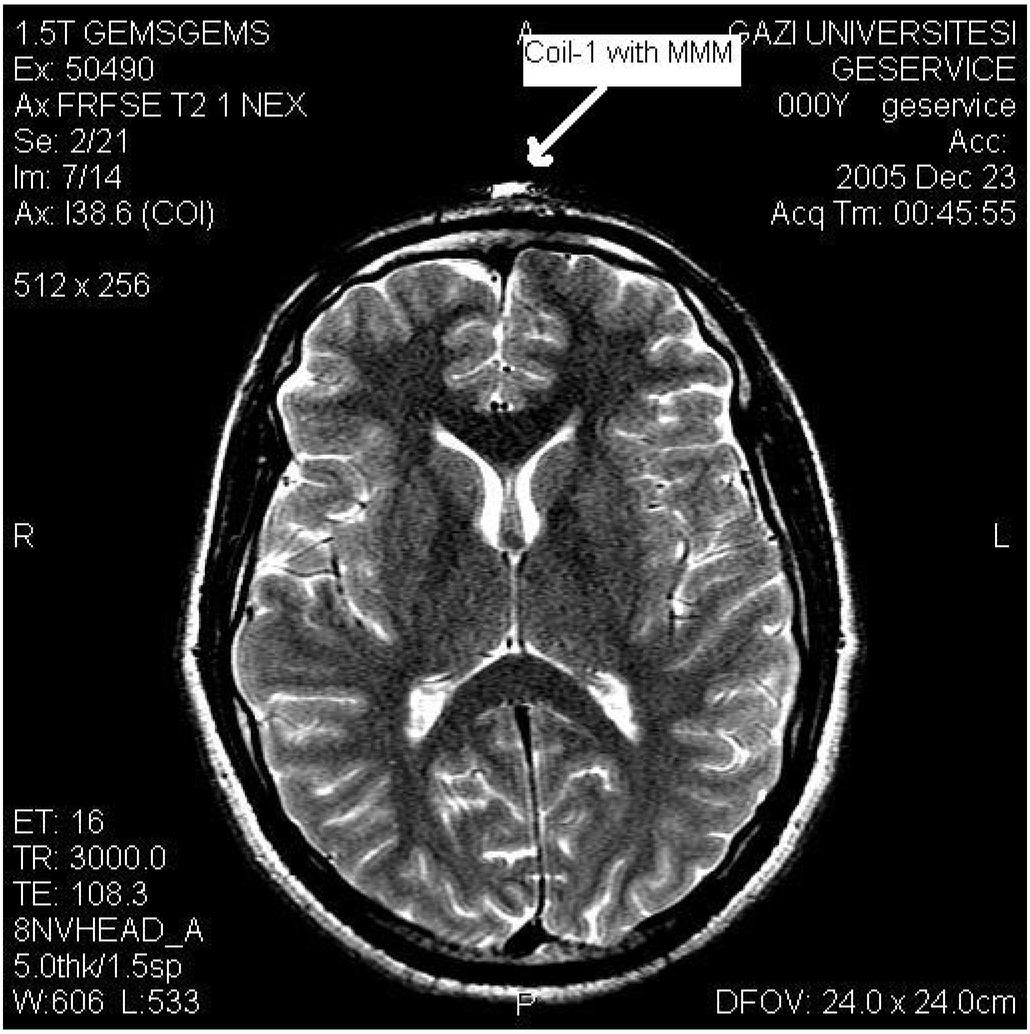

Figure 4.5: Coil-1 with Multi-Modality Marker. ICRF coil increased signal intensity significantly.

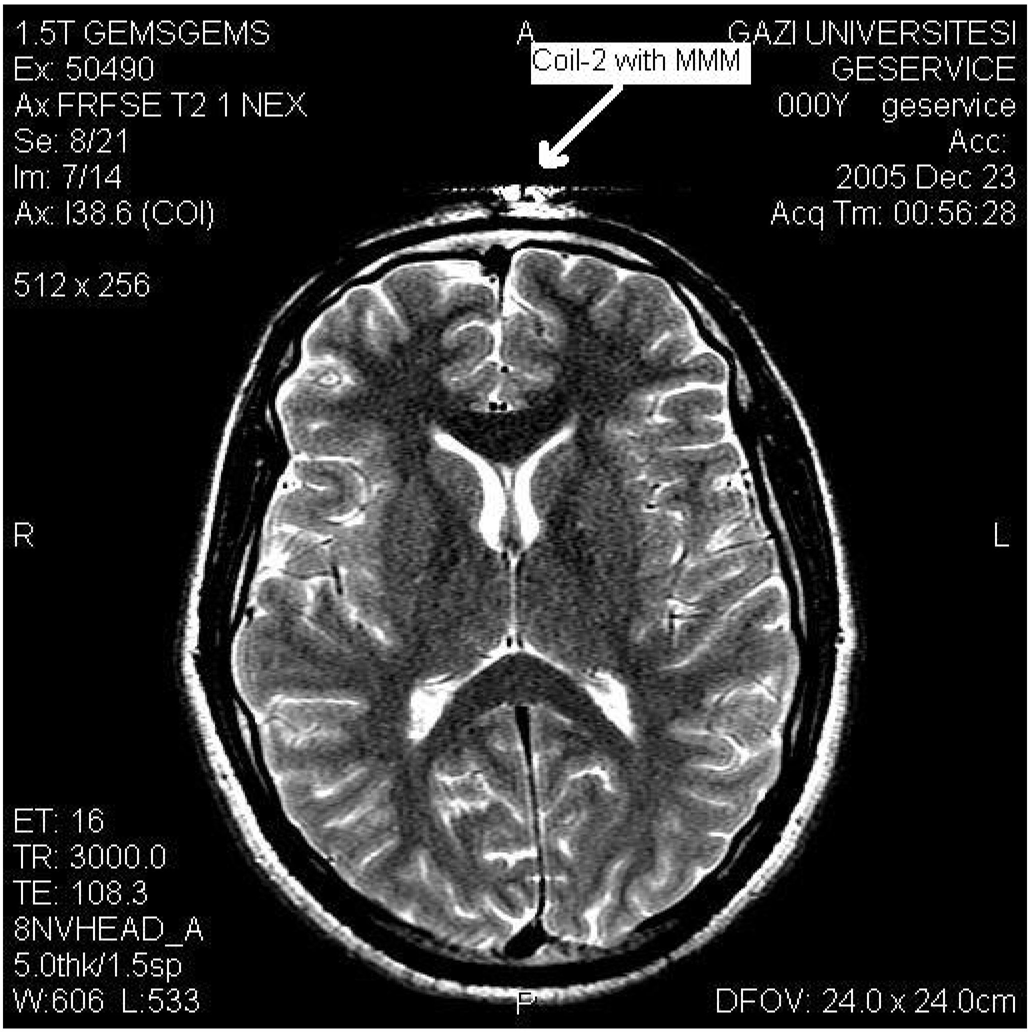

Figure 4.6: Coil-2 with Multi-Modality Marker. ICRF coil increased signal intensity so that signal near the gel saturates.

Below, images have the same parameters as previous case, in addition, fat suppression is applied.

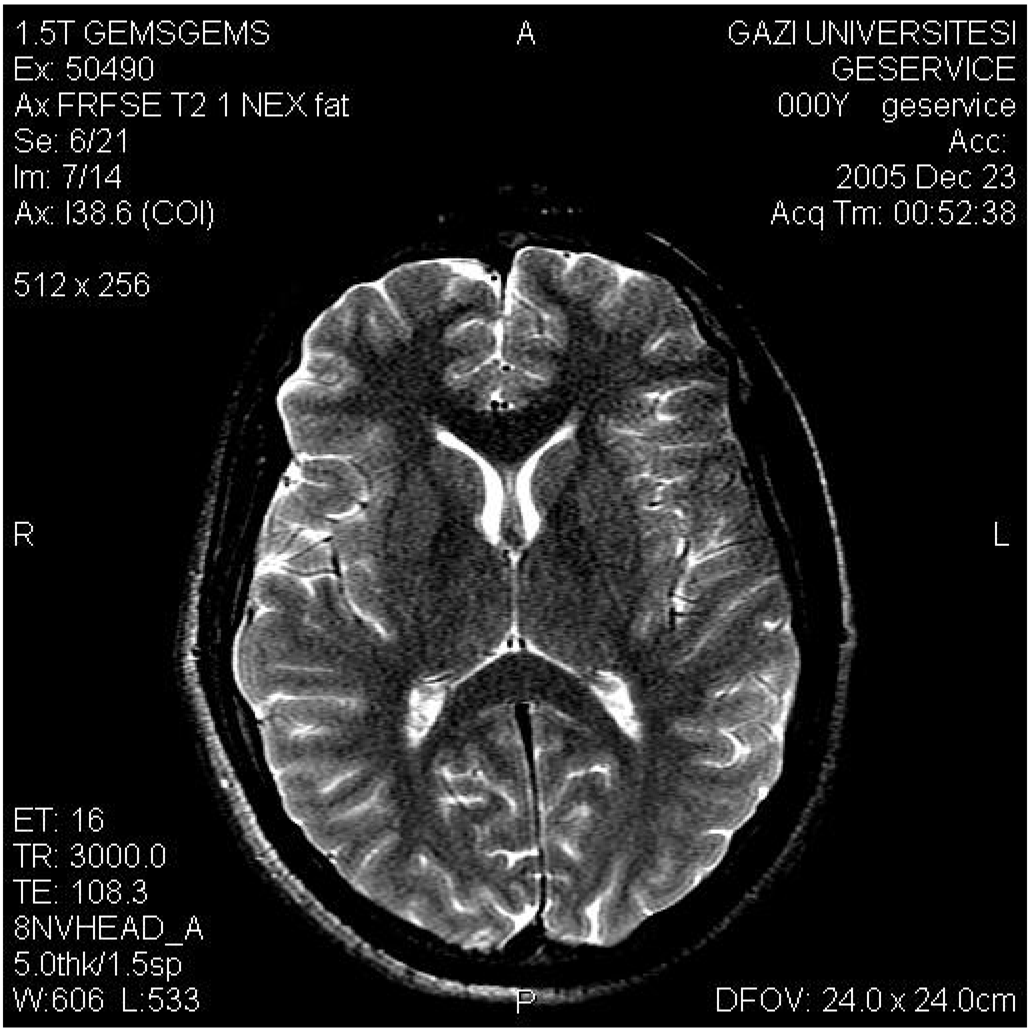

Figure 4.7: Coil-1 with Multi-Modality Marker. Marker cannot be seen in this sequence (T2 Weighted Fat Suppression).

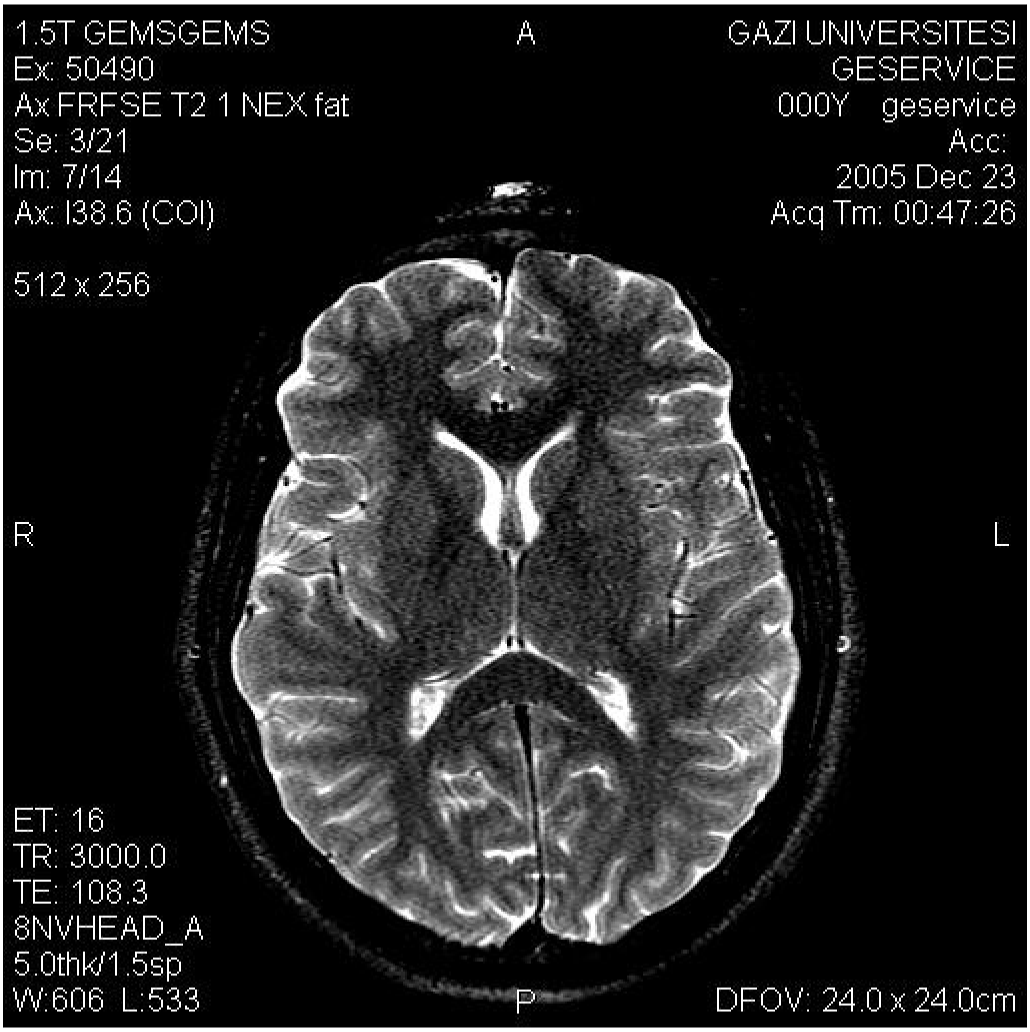

Figure 4.8: Coil-1 with Multi-Modality Marker.

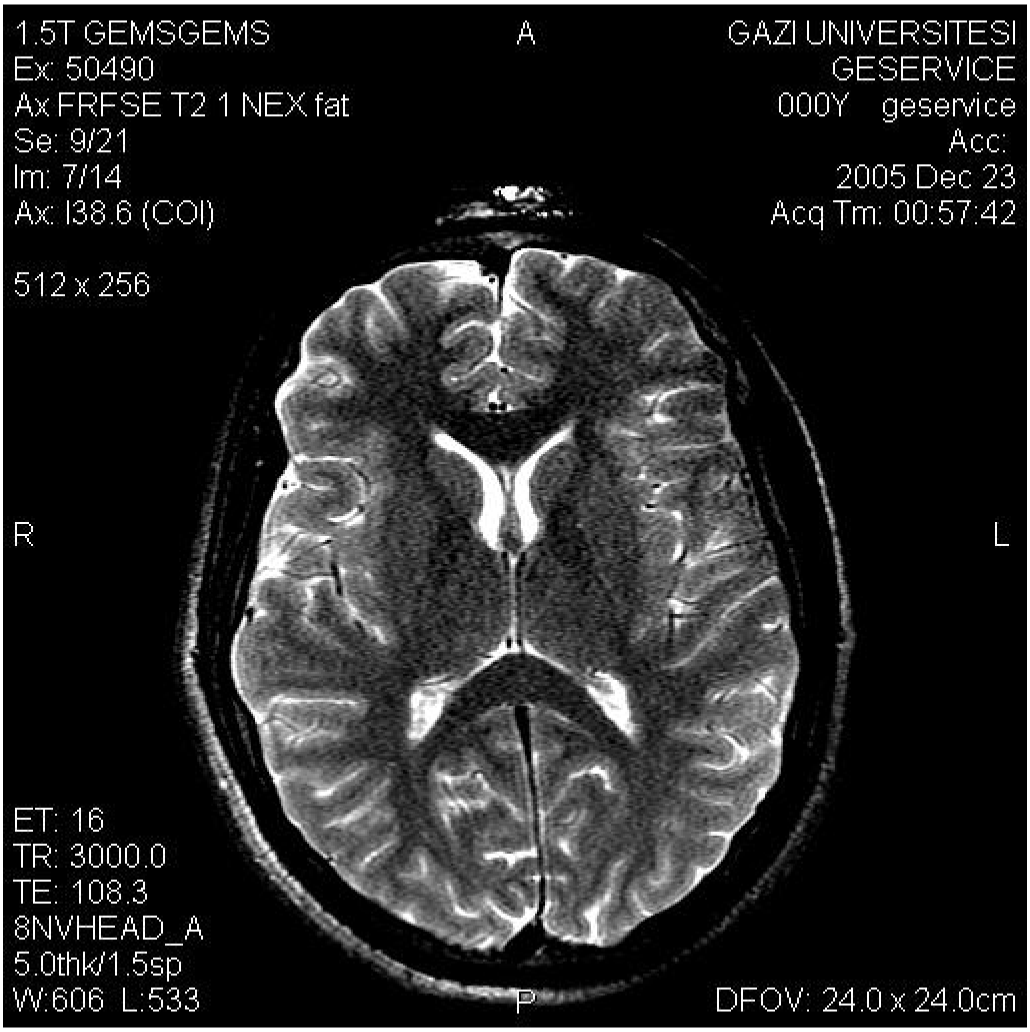

Figure 4.9: Coil-2 with Multi-Modality Marker.

4.6 Conclusion

We have demonstrated a novel method of image registration in image guided surgery. This new technique increased signal level of Multi-Modality Markers effectively.

5. EVALUATION OF INTERNAL MRI COILS USING ULTIMATE INTRINSIC SNR

5.1 Preface

This study was initiated by Imad Amin Abdel-Hafez, who completed an MS thesis on this topic in 2000. Project was restarted in 2003 as two senior projects, by Haydar Çelik and Yiğitcan Eryaman. Project was concluded in 2004 while both of them are in the graduate school. One journal paper and one conference abstact resulted out of this study. While Haydar Çelik became the first author of the journal paper, Yiğitcan Eryaman became the first author of the conference abstract., This chapter was reproduced from the journal publication (Reference: Celik H, Eryaman Y, Altintas A, Hafez IA, Atalar E. "Evaluation of Internal MRI Coils using Ultimate Intrinsic SNR". Magn Reson Med 52:640-649, 2004).

5.2 Introduction

In MRI, the performance of radiofrequency (RF) coils plays a critical role in determining the quality of acquired images. Optimum RF coil designs differ for different imaging locations in the body. Studies about optimum coil designs, however, have generally been performed for a given coil geometry (30,31).

There are various types of disposable internal coils, such as opposed solenoids (32,33), expandable coils (34-37), elongated loops (4), and loopless antennas (18), for use in various body cavities, including the vagina, esophagus (15), urethra (16), blood vessels (17,18), and rectum (19). Although there is an increase in the SNR of MRI images when these coils are used, it is not possible to make a direct comparison of the performance of internal coils with external coils. Furthermore, there is no formal method by which to evaluate the performance of these internal coil designs in terms of signal-to-noise ratio. Earlier, with a similar motivation, we calculated the ultimate value of the intrinsic SNR (UISNR) for external coils (12), where the intrinsic signal-to-noise ratio (ISNR) was defined for a given sample-coil combination as the MR signal voltage received from a unit volume of the sample divided by the root-mean-square (RMS) noise voltage received per square-root of bandwidth (8). Since the ultimate value of the intrinsic SNR is independent of coil design, the information obtained from the UISNR value can be used as a reference to potentially improve the performance of a coil.

In this paper, the calculation of UISNR was reformulated in order to extend it to internal MRI coils (38). The cylindrical body model is used for both UISNR values, in order to utilize cylindrical symmetry, and coordinates to represent EM fields propagating inside the body. This idea brings simplicity, and does not affect the result negatively. This model has been used by other researchers (30,39,40), and the results obtained with this model are consistent with previous work. A cylindrical body model with uniform electromagnetic (EM) properties was used to approximate the human body (see Figure 5.1).

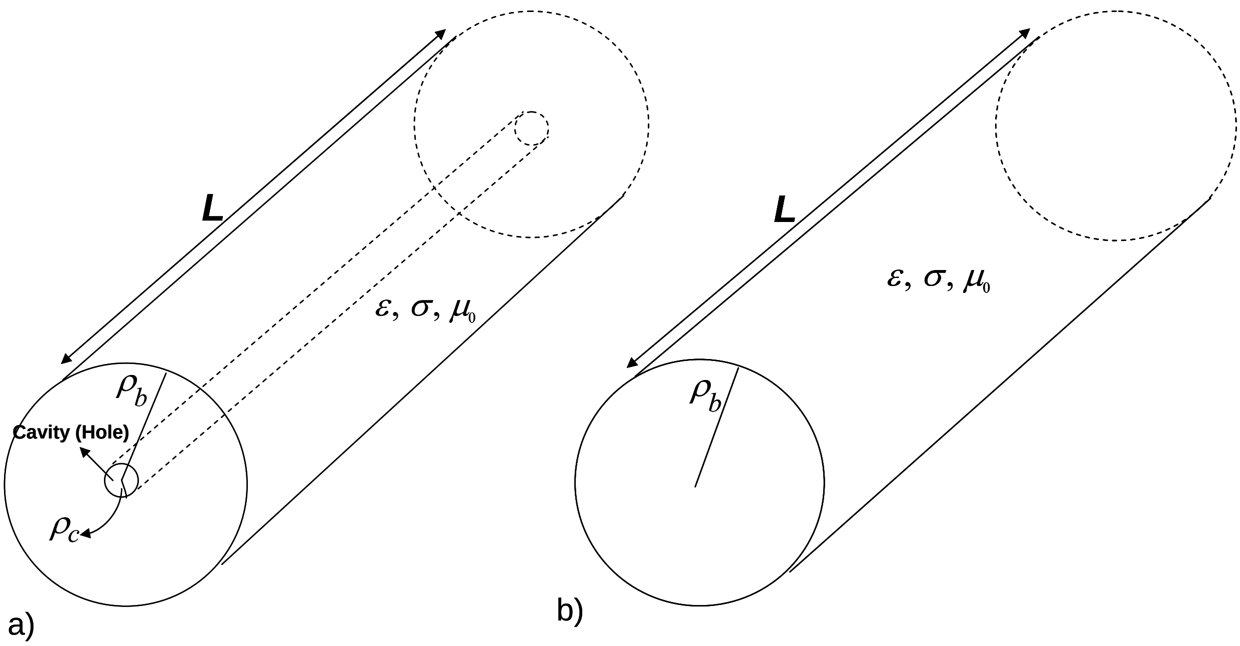

Figure 5.1: **a)** Cylindrical body model with a coaxial cavity. This model is used for obtaining the UISNR values of an internal and external coil combination. **b)** A cylindrical body model without a cavity.

In this model, a co-axial cylindrical cavity is assumed to exist at the center of the body, simulating blood vessels or similar structures in which internal RF coils can be placed. With this structure, while surface (or external) RF coils can be placed on the exterior surface of the body, internal coils can be placed in the central cavity.

In order to obtain the signal and noise voltages picked up by a receiving coil, one can use the reciprocity principle and determine the electromagnetic fields generated by the receiving coil when it is used as a transmitter (39). By assuming that body noise is dominant among other sources of noise, and with the constraint of having a fixed value of the forward polarized component of the magnetic field at the point of interest, SNR can be maximized by minimizing the total power deposited in the body (12). Therefore, for a given point of interest and electromagnetic (EM) properties of the body, the optimum electromagnetic field distribution must be calculated. As will be shown, this is not only a more general problem than the parametrical optimization of a given coil structure, but also a much easier problem to solve.

The UISNR values for various frequencies and cavity sizes were calculated. The results were used to measure the performance of a loopless antenna (18) and an endourethral coil (16) in the cavity.

5.3 Theory

In the calculation of the ultimate value of the SNR, optimization of the associated electromagnetic field was performed rather than the optimization of a specific coil geometry (12). UISNR depends on the geometrical and electrical properties of the body and the position of the point-of-interest. We assumed a cylindrical body and the electromagnetic fields inside the human body to be expressed as a weighted sum of the cylindrical waves, which serve as basis functions. To obtain the UISNR value, the noise level in the system should be considered. Power losses, such as conductor losses, radiation losses, and body losses, primarily determine the noise level. For a system with well-designed RF coils, conductor losses and radiation losses can be minimized and the body loss remains the main factor that limits the SNR value. The expression for the intrinsic signal to noise ratio (8,12), which is independent of imaging parameters, is as shown below,

$$\Psi = \frac{\sqrt{2}\omega \mathrm{M}_0}{\sqrt{4k_b \mathrm{T}R}} B_f \qquad [12]$$

where k_b is the Boltzmann's constant, T is the sample temperature, ω is the Larmour frequency, and M_0 is the instantaneous magnetic moment per sample voxel immediately after applying a 90^0 degree pulse. B_f is the forward polarized magnetic field component and is defined as $B_f = \mu H_f$, where μ is the magnetic permeability and $H_f = \left(H_\rho - iH_\phi\right)/\sqrt{2}$ when the main magnetic field is along the +z direction and for a time convention of $e^{j\omega t}$ (suppressed), where i is the complex number $\sqrt{-1}$. Magnetic permeability in the body is assumed to be uniform and equal to the permeability of free space, μ_0. R is the real part of the input impedance seen by the input terminals of the coil. From the reciprocity principle (39,41), the value of R can be found by calculating the total dissipated power when the receiver coil is used as a transmitter and driven by a 1 amp rms current source from its input terminals.

As mentioned above, the body loss, R_{body}, is the main factor in power dissipation and noise level. For a properly designed system $R \cong R_{body}$ and with a unit rms current excitation, it becomes $R_{body} = P_{loss}$, where P_{loss} is power loss in the body. We assume that outside the body, we have a lossless region; thus, there is no contribution to power dissipation from the fields in the outside region. Since we do not specify the fields outside the body, we do not need to impose boundary conditions.

In order to obtain maximum SNR, R_{body} must be minimized, while H_f must be maximized. Since, with the aid of a simple transformer, the value of H_f can be modified without affecting the SNR, in our calculations, we arbitrarily assumed the forward polarized magnetic field at the point of interest, $\vec{\mathbf{r}}_0$, is fixed to 1, i.e., $H_f(\vec{\mathbf{r}}_0) = 1$. Therefore, the problem of calculation of the ultimate value of the intrinsic SNR (UISNR) reduces to minimization of R_{body} (12).

5.3.1 Electromagnetic Field Expression for a Cylindrical Body

For an infinitely long cylindrical body, the electromagnetic fields can be written in terms of an inverse Fourier transform of cylindrical wave function expansions (39). When one considers a cylindrical body of finite length, the Fourier integral becomes the Fourier series at discrete spectral values. For the problem considered here, the optimum electromagnetic (EM) field that will minimize power dissipation inside the body can be written as the weighted sum of the cylindrical waves:

$$\vec{\mathbf{E}} = \sum_{m=-\infty}^{\infty} \sum_{n=-\infty}^{\infty} \vec{\mathbf{E}}_{mn} \qquad [13]$$

where m and n are integer variables representing the Fourier modes (Fourier components).

The cylindrical waves can be generated from the z-components of electric and magnetic field intensities, which are the solutions for scalar Helmholz equations:

$$E_{zmn} = (A_{mn} J_m(\beta_{\rho n}\rho) + C_{mn} Y_m(\beta_{\rho n}\rho))\, e^{jm\phi} e^{-j\beta_{zn} z} \qquad [14]$$

$$H_{\mathrm{zmn}} = -j(B_{mn} J_m(\beta_{\rho n}\rho) + D_{mn} Y_m(\beta_{\rho n}\rho))\, e^{jm\phi} e^{-j\beta_{zn} z} \qquad [15]$$

where ε is the electric permittivity, and J_m and Y_m are mth order first and second kinds of Bessel functions, respectively (the second kind of Bessel functions are also called Neumann functions). In addition, A_{mn}, B_{mn}, C_{mn}, and D_{mn} are the unknown weights that need to be determined and $\beta_{\rho n}$ is given by

$$\beta_{\rho n} = \sqrt{\beta^2 - \beta_{zn}^2} \tag{16}$$

where $\beta^2 = -j\omega\mu_0\left[\sigma + j\omega\varepsilon\right]$. Note that β is the wave number in the body and σ is the conductivity of the body. In general, β_z comprises a continuous spectrum of cylindrical waves (39). The field representation above is an alternative to the eigenfunction (modal) representation. They are related through an integration in the complex β_z plane (42). Due to the finite length of the body, β_z is limited to a discrete set of real numbers as $\beta_{zn} = \left(2\pi / L\right)n$, where L is the length of the body and n is an integer value both positive and negative, corresponding to the Fourier series expansion of the fields. Thus, the EM field becomes periodic along the *z* direction with a period of *L*. We will later show that our results do not depend on the value of *L*, as long as *L* is large enough.

Using Maxwell's equations, the other components (ϕ and ρ) of the fields in Eq. [13] can be obtained in terms of E_z and H_z. As an example, consider the two equations below:

$$\frac{\partial E_z}{\partial \phi} - \rho\frac{\partial E_\phi}{\partial z} = -j\omega\mu\rho H_\rho \tag{17}$$

and

$$\frac{\partial H_\rho}{\partial z} - \frac{\partial H_z}{\partial \rho} = (\sigma + j\omega\varepsilon)E_\phi \tag{18}$$

Differentiating Eq. [17] with respect to z and substituting into Eq. [18] gives E_ϕ and H_ρ components of the field (see Appendix A. For other components, refer to Maxwell's equations in (43)). It should be noted that the field expansions are valid for all types of electromagnetic sources. The unknown weights take specific values for a given configuration.

Since $e^{-j(2\pi/L)nz}$ and $e^{jm\phi}$ terms are common in all field expressions, for convenience $\vec{E}_{mn}$ can be expressed as:

$$\vec{E}_{mn} = \mathbf{E}_{mn} \cdot \vec{\boldsymbol{\alpha}}_{mn} \cdot e^{jm\phi} e^{-j(2\pi/L)nz} \qquad [19]$$

where

$$\vec{\boldsymbol{\alpha}}_{mn} = [A_{mn}\ B_{mn}\ \mathrm{C}_{mn}\ D_{mn}]^T \qquad [20]$$

and $\mathbf{E}_{mn}$ is a 3-by-4 matrix, and is a function of ρ, but not ϕ or z. In Eq. [20], T denotes a transpose operation.

5.3.2 Power Deposited in the Body

The main reason for considering the electromagnetic field as a weighted Fourier sum of cylindrical waves is to find the optimum field, which will minimize the power consumption in the body model. Each cylindrical wave expression serves as a basis function in the expansion of the optimum field. The total power deposited in the body, which is also equal to R_{body}, can be calculated as a volume integral as shown below:

$$R_{body} = \sigma \int_{body} \vec{\mathbf{E}}^{*T} \vec{\mathbf{E}} d\upsilon \qquad [21]$$

where (*) above the electric field denotes the conjugate operator and $d\upsilon$ is the differential volume element inside the volume determined by the body model. Note that the conductivity, σ, is taken as uniform throughout the body.

When the field is expressed as the sum of cylindrical waves (see Eq.

[13]), the integral becomes:

$$R_{body} = \sigma \int_{body} \left(\sum_{mn} \vec{\mathbf{E}}^{*T}_{mn} \right) \cdot \left(\sum_{kl} \vec{\mathbf{E}}_{kl} \right) d\upsilon \qquad [22]$$

where *k* and *l* are integers. If the summation is taken out of the integral operator, R_{body} can be written as:

$$R_{body} = \sum_{mn} \sum_{kl} \sigma \int_{body} \vec{\mathbf{E}}^{*T}_{mn} \cdot \vec{\mathbf{E}}_{kl} d\upsilon \qquad [23]$$

The right-hand side of the above equation is a volume integral and involves integration with respect to ρ, ϕ, and z variables.

The forward polarized magnetic field, $H_f\left(\vec{\mathbf{r}}\right)$ can be expressed as:

$$H_f\left(\vec{\mathbf{r}}\right) = \sum_{mn} \vec{\mathbf{b}}_{mn}\left(\vec{\mathbf{r}}\right) \cdot \vec{\boldsymbol{\alpha}}_{mn} \qquad [24]$$

where $\vec{\mathbf{b}}_{mn}\left(\vec{\mathbf{r}}\right)$ is a row vector and $\vec{\mathbf{r}} = \left(\rho, \phi, z\right)$ denotes the position of the point of interest in the cylindrical coordinates. The components of $\vec{\mathbf{b}}_{mn}\left(\vec{\mathbf{r}}\right)$ are expressed in terms of the components of the magnetic field, as shown in Appendix B.

5.3.3 Ultimate Intrinsic SNR for Internal and External Coil Combination

In the calculation of UISNR, we assumed a cylindrical object with a co-axial cavity, as shown in Figure 5.1a. It is assumed that there is no electrical loss in the cavity and outside this cylindrical object and all the losses are due to finite conductivity of the object. This structure permitted placement of both internal coils in the cavity and external coils on the surface of the object. Therefore, the following calculation applies to the UISNR for an internal and external coil combination.

Because of the cylindrical symmetry of this object, this volume integral in the above equation can be decomposed into three integrals:

$$\int_{body} \vec{\mathbf{E}}_{mn}^{*T} \cdot \vec{\mathbf{E}}_{kl} d\upsilon = \int_{\rho_{cavity}}^{\rho_{body}} (\mathbf{E}_{mn} \cdot \vec{\boldsymbol{\alpha}}_{mn})^{*T} \cdot (\mathbf{E}_{kl} \cdot \vec{\boldsymbol{\alpha}}_{kl}) \rho d\rho \int_{0}^{2\pi} e^{-j(m-k)\phi} d\phi \int_{-L/2}^{L/2} e^{-j(2\pi/L)(n-l)z} dz$$

[25]

where, ρ_{cavity} and ρ_{body} are the hole (cavity) and body radii, respectively (see Figure 5.1a). Because we only considered the region interior to the body, limits for integration, with respect to the ρ variable, were determined by the cavity and body radii. Note that L is the limit of integration with regard to the z variable. The complexity of the body integral can be reduced by evaluating the integrals with respect to the variables ϕ and z. With this simplification, the body integral can be written as follows:

$$\int_{body} \vec{\mathbf{E}}_{mn}^{*T} \cdot \vec{\mathbf{E}}_{kl} d\upsilon = \begin{cases} 2\pi L \vec{\boldsymbol{\alpha}}_{mn}^{*T} \cdot \left[\int_{\rho_{cavity}}^{\rho_{body}} \mathbf{E}_{mn}^{*T} \cdot \mathbf{E}_{kl} \rho d\rho \right] \cdot \vec{\boldsymbol{\alpha}}_{kl}, & \text{if } m=k \text{ and } n=l \\ 0 \quad , & \text{elsewhere} \end{cases}$$

[26]

The above equation shows that all modes are orthogonal to each other. This simplification makes it possible to express the R_{body} as a summation in m and n only, as below

$$R_{body} = \sum_{mn} p_{mn} \qquad [27]$$

where

$$p_{mn} = 2\pi L \sigma \vec{\boldsymbol{\alpha}}_{mn}^{*T} \cdot \left[\int_{\rho_{cavity}}^{\rho_{body}} \mathbf{E}_{mn}^{*T} \cdot \mathbf{E}_{mn} \rho d\rho \right] \cdot \vec{\boldsymbol{\alpha}}_{mn} \qquad [28]$$

The new variable p_{mn} denotes the power dissipation for each of the modes, and is also equal to:

$$p_{mn} = \vec{\boldsymbol{\alpha}}_{mn}^{*T} \cdot \mathbf{R}_{mn} \cdot \vec{\boldsymbol{\alpha}}_{mn} \qquad [29]$$

where

$$\mathbf{R}_{mn} = \left[2\pi L\sigma \int_{\rho_{cavity}}^{\rho_{body}} \mathbf{E}_{mn}^{*T} \cdot \mathbf{E}_{mn} \rho d\rho \right] \qquad [30]$$

It is important to note that $\mathbf{R}_{mn}$ is a Hermitian matrix. This fact simplifies the calculations, since it requires the computation of the terms only on one side of the diagonal.

The problem of finding the ultimate value of SNR becomes that of finding the optimum $\vec{\boldsymbol{\alpha}}_{mn}$ values, such that:

$$R_{\min} = \sum_{mn} \vec{\boldsymbol{\alpha}}_{opt_{mn}}^{*T} \cdot \mathbf{R}_{mn} \cdot \vec{\boldsymbol{\alpha}}_{opt_{mn}} \qquad [31]$$

with the constraint that $H_f(\vec{\mathbf{r}}_0) = 1$. This constrained minimization problem can be solved using standard techniques such as the Lagrange multiplier technique and $\vec{\boldsymbol{\alpha}}_{opt_{mn}}$ can be found as:

$$\vec{\boldsymbol{\alpha}}_{opt_{mn}} = \mathbf{R}_{mn}^{-1} \cdot \vec{\mathbf{b}}_{mn}^{*T}\left(\vec{\mathbf{r}}\right) R_{\min} \qquad [32]$$

where

$$R_{\min} = \frac{1}{\sum_{mn} G_{mn}} \qquad [33]$$

and

$$G_{mn} = \vec{\mathbf{b}}_{mn}\left(\vec{\mathbf{r}}\right) \cdot \mathbf{R}_{mn}^{-1} \cdot \vec{\mathbf{b}}_{mn}^{*T}\left(\vec{\mathbf{r}}\right) \qquad [34]$$

Although m and n values are unbounded, for practical computational purposes, they need to be limited to a range, and the selection of the proper range will be discussed later.

It is instructive to note that, as L increases, the element values of the $\mathbf{R}_{mn}$ matrix increase as well; thus, G_{mn} decreases. On the other hand, the density of the samples of β_z (note that $\beta_{zn} = (2\pi / L)n$) increases with L. As a result, the value of $R_{\min}$ becomes independent of L, for sufficiently large values of L.

Once the optimum weights are known for a given point of interest, the forward polarized magnetic field (H_f) inside the human body model can also be simulated to show the sensitivity distribution of the optimum coil.

5.3.4 Ultimate Intrinsic SNR for Solely External Coils

In the same cylindrical geometry, if one removes the cavity (see Figure 5.1b), the calculation of UISNR will be solely for external coils since there will be no cavity in which to place an internal coil. In this case, we will need to make some small modifications to the above formulation.

First, ρ_{cavity} must be set to zero. Therefore, the boundaries of the integrations in Eqs. [25], [26], and [28] should be changed to 0 to ρ_{body}. This change will render Neumann functions inapplicable, because Neumann functions have singularities at the origin. Therefore, C_{mn} and D_{mn} must vanish. As a result, in the calculation of the UISNR for external coils, only Bessel J-type functions should be included in the expressions.

Apart from these distinctions, the calculation of UISNR for external coils is identical to the calculation of UISNR for the internal and external coil combination.

5.4 Simulations and Results

A MATLAB (version 6.0,Mathworks Inc., Natick, MA) program was developed to calculate the UISNR values. In all calculations, a uniform conductivity σ of 0.37 $\Omega^{-1}m^{-1}$, a relative electric permittivity ε_r of 77.7, and a relative magnetic permeability μ_r of 1.0 are taken as average values at 64 MHz (or 1.5 T for protons) (12). The SNR calculations in (44) for the loopless antenna (18) and experimental results for the endourethral coil design (16) were compared with the UISNR values.

5.4.1 Optimum Sensitivity Distribution

The reason for using an internal coil is to obtain better results compared to external coils. For this purpose, sensitivity distribution maps, i.e., the distribution of the forward polarized magnetic field, are used to ensure the dominant effect of the internal coil. In order to demonstrate the distribution, both axial and sagittal views were obtained. We call these distribution maps H-maps. First, a logarithmic intensity scale is employed on the $z = 0$ plane with respect to ϕ and ρ (axial H-map). The point of interest was chosen on the $z = 0$ plane as well. The map was enlarged 100 times to concentrate on a smaller field of view and to observe the effect of the internal coil. In Figure 5.2, the white cloud around the cavity represents high field magnitudes.

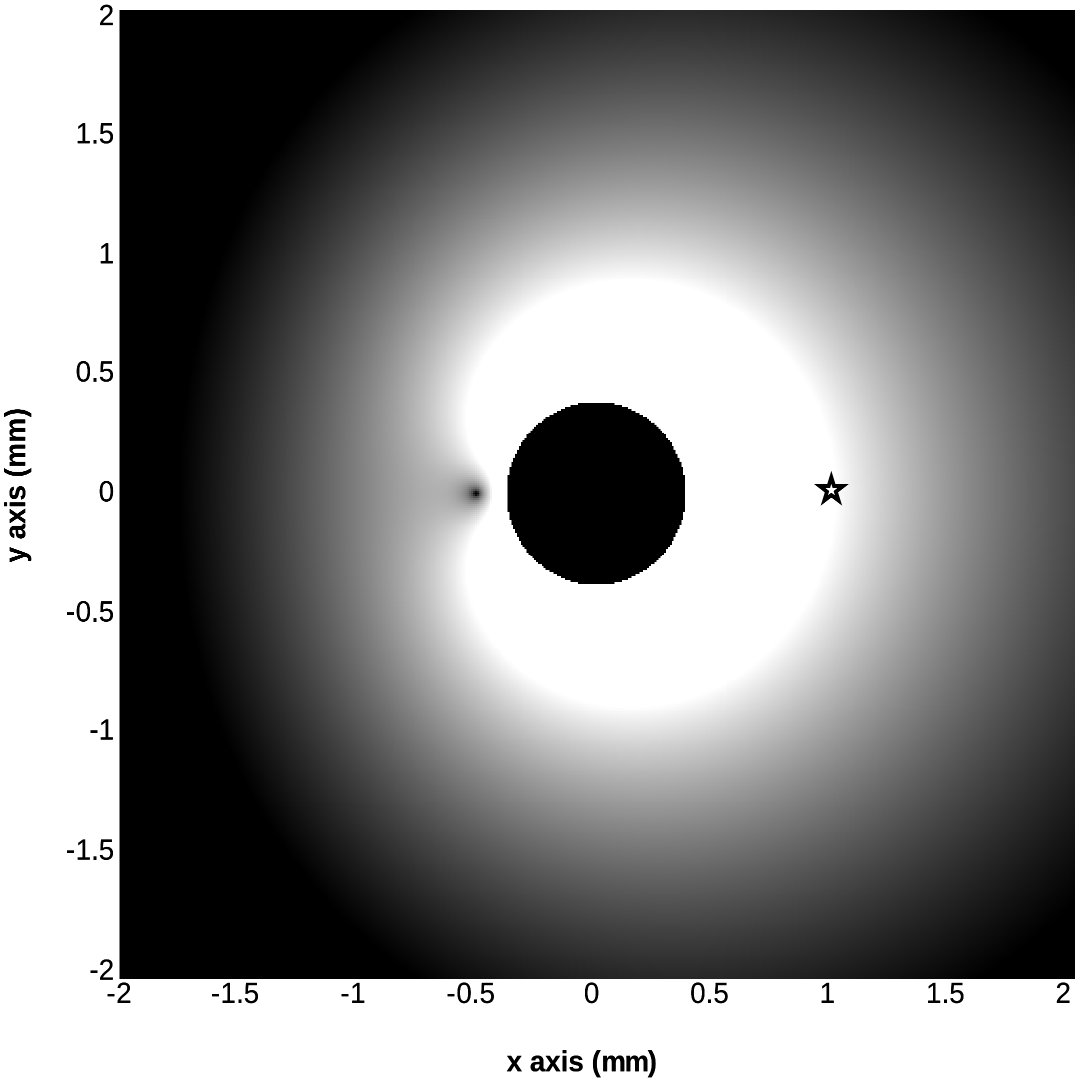

Figure 5.2: Signal reception profile of optimum internal coil (axial H-map). This shows the optimum field pattern inside the body model that will maximize the intrinsic SNR at location $(\rho=1\text{ mm}, \phi=0, z=0)$. A logarithmic intensity scale is employed.

As is clear from the same figure, the field is concentrated around the cavity (which is shown in black in the middle of the image) but also shifted toward the point of interest. A sagittal H-map is another perspective for a signal reception profile of the optimum internal coil, obtained on the $\phi = 0$ plane, at the point of interest $(\rho = 1 \text{ mm}, \phi = 0, z = 0)$ indicated by a star (see Figure 5.3a).

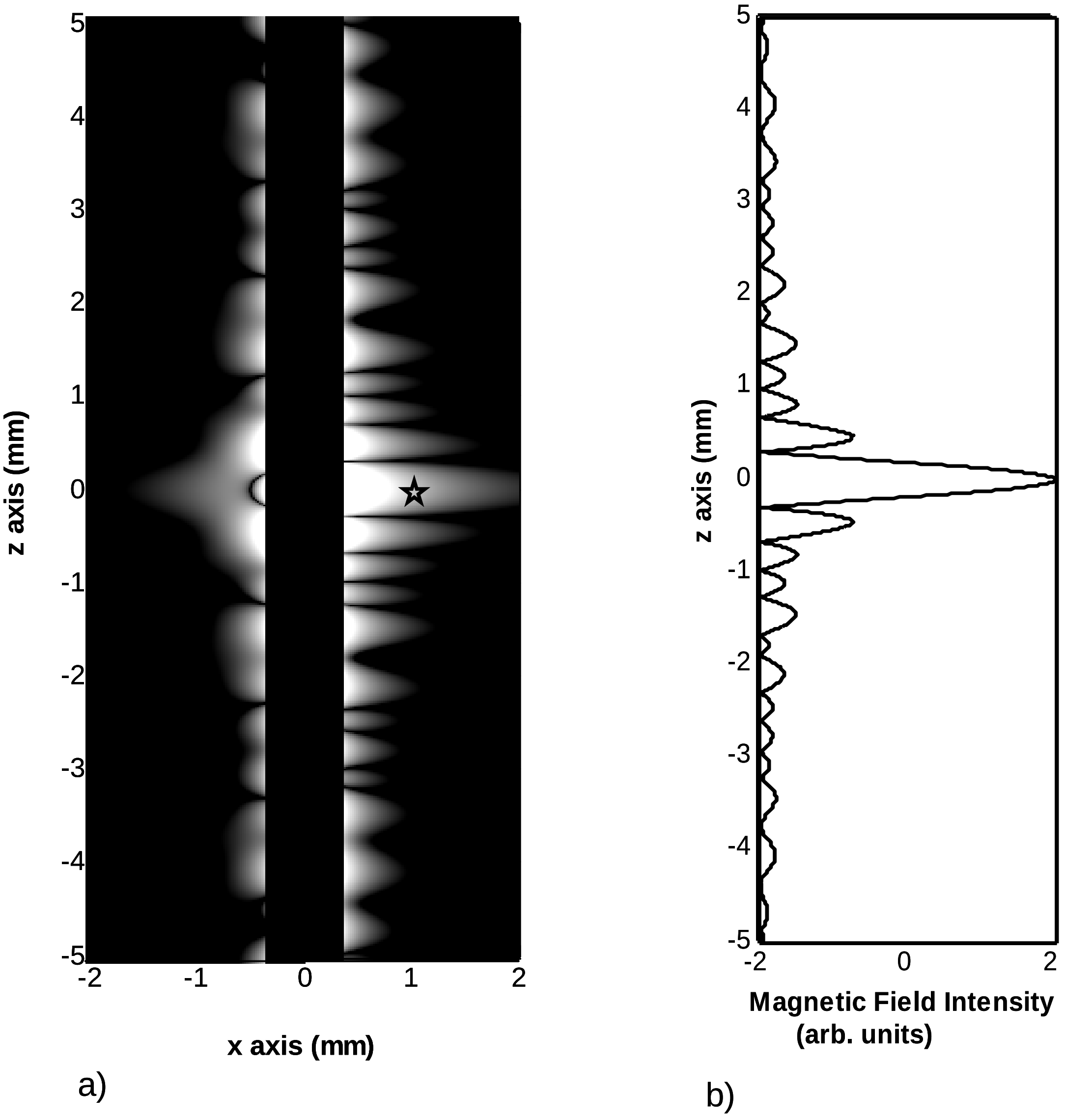

Figure 5.3: **a)** Sagittal H-map for the optimum coil. This map is produced on the plane, ϕ = 0, and the point of interest located at $(\rho = 1 \text{ mm}, \phi = 0, z = 0)$ is indicated by a star. A logarithmic intensity scale is employed. **b)** Sensitivity magnitude profile for the optimum coil. H_+ field sensitivity is plotted at $x = 1$ mm in arbitrary units. Both figures show that most of the field energy is concentrated in a narrow

region on the z axis and the greatest brightness indicates where the position of the internal coil should be.

Again, a logarithmic intensity scale is employed and enlarged to a smaller field of view. The highest brightness, which shows where the position of the internal coil should be located, occurs approximately between -1 mm and 1 mm on the z direction. Beyond this region, the field is very small with regard to the field at the center, $z=0$ plane. The point of interest is indicated by a star and is in the cloud (white region) that represents the field of the internal coil. The appearance of the optimum magnetic field distribution is in line with intuition. In Figure 5.3b, the sensitivity is plotted at $x=1\text{ mm}$. Both figures indicate that most of the field energy is concentrated in a small region on the z-axis, if we ignore some fluctuations caused, most probably, because of the truncation of the modes.

5.4.2 Accuracy Analysis

In our calculations, some assumptions were used. These assumptions may cause inaccuracy in the results. A detailed analysis of these error sources is necessary.

The length of the body is an important parameter, because, in the formulation, we assumed that the optimum EM field is periodic with the length of the cylinder. Here, we need to verify that this periodicity assumption does not alter the solution significantly. With this purpose, first, body length, *L,* was taken as 1 m and SNR was calculated for a point of interest $(\rho=1\text{ cm},\ \phi=0,\ z=0)$. Then, the result was compared with the SNR value for an *L* equal to 2 m and for the same point of interest. Note that in order to keep the range of β_z constant, the number of *n* modes was doubled. There was only a 1% difference between these two results. The same procedure was repeated for different points of interest, and the SNR value did not change more than 1%. Note that at the end of the theory section, it is explained that $R_{\min}$ is independent of L when L is large. This result is concordant with the result above.

Although an infinite number of m and n indices are necessary for an exact result, a restricted number of Fourier modes provides an accurate solution. Thus, in order to check whether there are enough modes, G_{mn} values are shown in the form of a map (the m and n are the coordinates of the map), which is useful for showing the importance of each mode used for the numerical calculation of the UISNR. We call this map a G-map (see Figure 5.4). Note that only positive n values are shown because of the symmetry of the problem, i.e., $G_{mn} = G_{m(-n)}$.

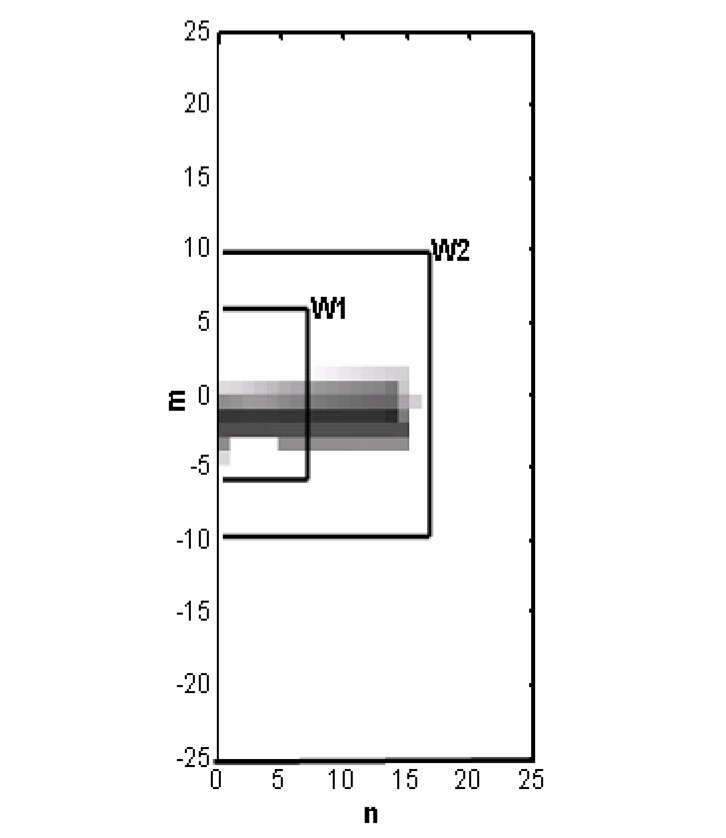

Figure 5.4: Relative importance of the modes (G-map).This is used for the numerical calculation of the UISNR. The weights of each mode were mapped on the horizontal and vertical axis, representing the m and n modes. The restriction of the

modes to those encompassed by bound W2 speeds the calculation with a negligible loss of accuracy (< 1%), whereas use of the overly-restrictive bound W1 results in a 33% error.

The necessary number of modes is decided by investigating the G-map with respect to the variable, n. The number of modes is decided according to the parameters of the body. For example, the number of modes increases as body length increases. We also observe that as the point of interest gets closer to the boundaries, a greater number of modes in m and n indices are needed. Although this is the case for most points of interest, the values that determine body resistance, and eventually the UISNR values, are limited to a small range of m and n values; therefore, a finite sum of selected modes is acceptable. In Figure 5.4, the total number of modes for both m and n is 1250, which is very high. Including all of these modes is time consuming. If smaller m and n values are chosen, the window will get smaller, as seen on W1 and W2. For window 1 (W1), the numbers of m and n are insufficient, and the UISNR value obtained for this window (where m = 6 and n = 7) is 33% less than the UISNR value of the largest window (m = 50, n = 25). However, W2 (m = 10, n = 17) provides almost the same UISNR value (a difference of 0.2%) as the largest window; thus, W2 includes the most effective modes and also takes much less time to plot the map. As a result, this mapping method is useful for efficient calculation of the result.

5.4.3 Analysis of Loopless Antenna

The loopless antenna (18) is a very simple antenna design that has been investigated for use in MRI-guided vascular interventions (45). The design consists of a coaxial cable with an extended inner conductor. Comparing the UISNR values of internal and external coils with the ISNR values of the loopless antenna is important in understanding its performance. The UISNR value of the internal and external coil combination was plotted for a 20 cm-radius body with a 0.375 mm radius cavity as a function of the position of the point of interest in Figure 5.5.

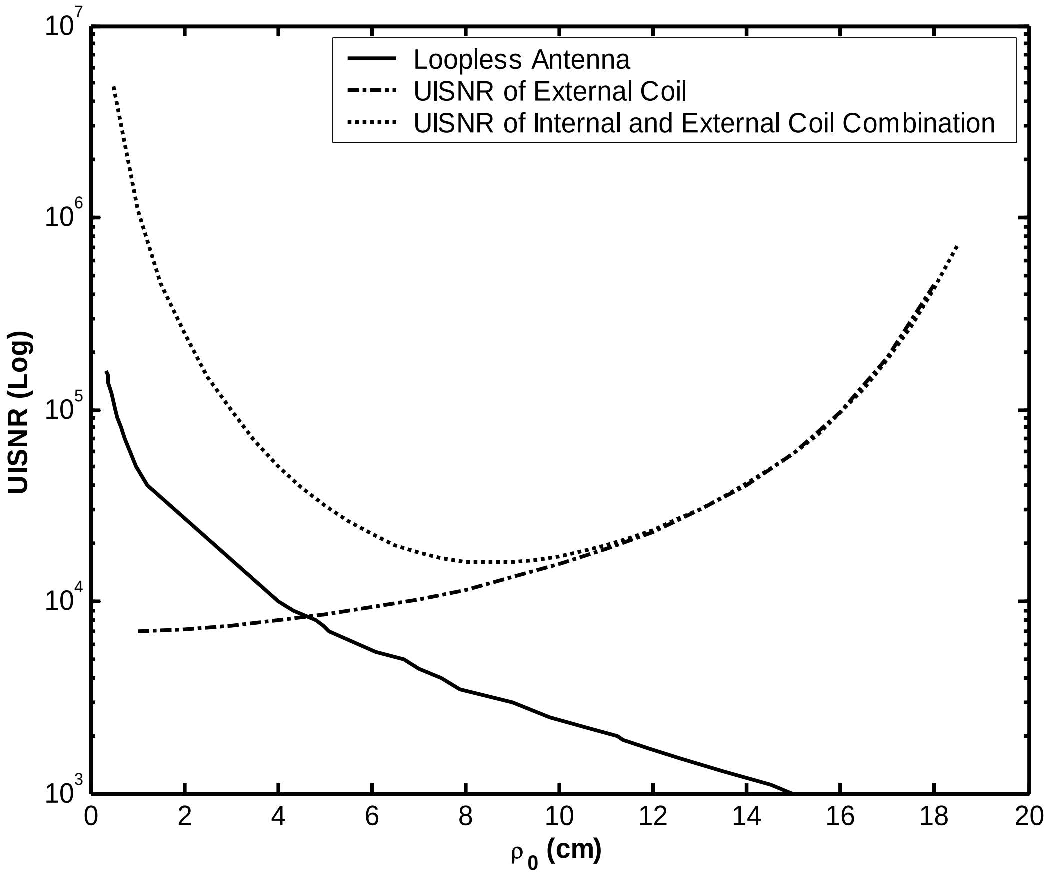

Figure 5.5. A comparison of three ISNR values. ρ_0 is the radial distance of the point of interest from the center of the object. The internal coil is effective at points near the cavity and then the external coil becomes effective as the point of interest approaches the outer boundary on the curve of the UISNR of an internal and external coil combination. In this figure, the external coil has a 20 cm body radius and the internal and external coil combination has a 20 cm body and a 0.375 mm cavity radii. The radius of the loopless antenna is 0.375 mm.

In the same graph, the intrinsic SNR value of a loopless antenna (44) and the UISNR value that can be obtained from exclusively external coils were plotted. By investigating this plot, one can understand how much room for improvement there is in the SNR performance of the loopless antenna. In addition, we can see in what region which coil performs better. For example, at a point of interest $(\rho = 1 \text{ mm}, \phi = 0, z = 0)$, the performance of the loopless antenna is only 4% of the UISNR of an internal and external coil combination. This means that there may be an internal MRI coil design that fits in the same cavity and performs 25 times better than the loopless antenna for that point of interest. It is important to note that the coil design that can result in this significant improvement is not known at this time.

Deciding whether to use the loopless antenna for a specific point of interest is crucial with regard to time saving and therapeutic management. In Figure 5.5, the SNR curve of the loopless antenna and the UISNR of the external coil intersect at one point. This point determines the radius of the "useful region" of an internal MRI coil, the loopless antenna. For points that are closer to the external surface of the body, some external coils, which perform better than the internal coil, may exist. The size of the useful region of an internal coil depends on the body radius. When the body size is large, the useful region of the internal coil increases, whereas, when the body size is small, the internal coil becomes useful for imaging a smaller region. Figure 5.6 shows the radius of the useful area as a function of body size for the loopless antenna. To obtain this plot, the values of UISNR were calculated for external coils and the SNR of the loopless antenna was compared with these UISNR values as a function of body radius.

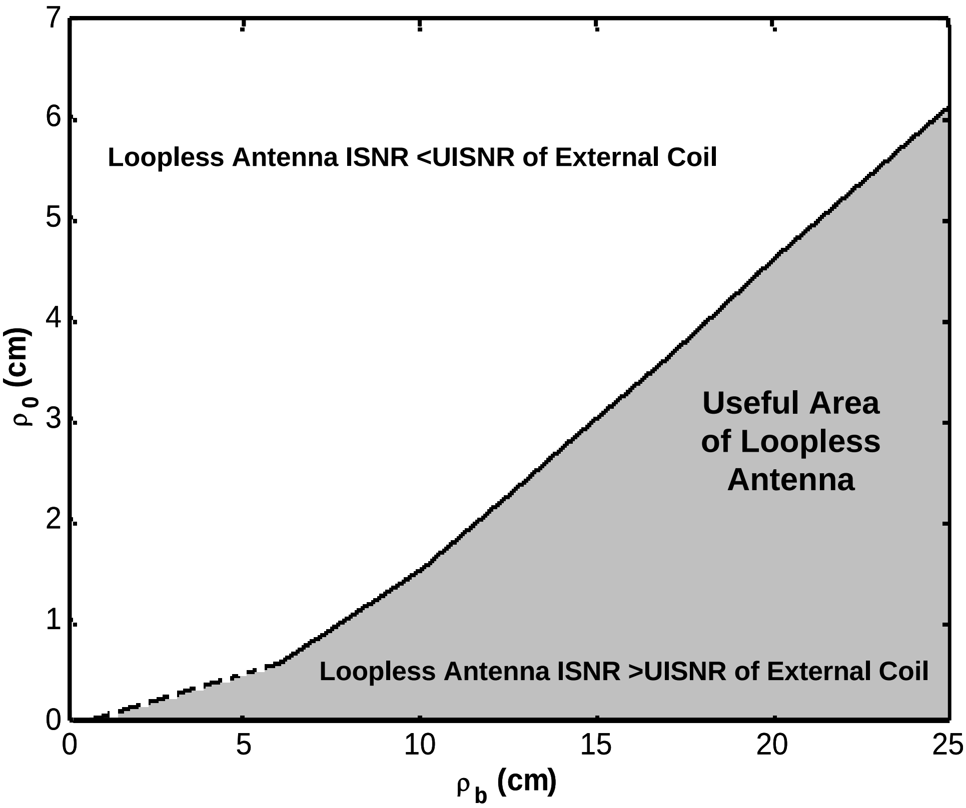

Figure 5.6: The useful area for the loopless antenna. The SNR values of the loopless antenna and the UISNR of the internal and external coil combination were compared for different values of body radius, ρ_b. For a given body radius, the loopless antenna outperforms the optimum external coil design for points of interest with ρ_0 values that fall in the shaded area. The region at the left bottom of the figure, shown by the dashed line, was found by interpolation.

For a fixed value of body radius, the SNR values were sampled at 5 mm, and the point where the loopless antenna SNR exceeded the UISNR for external coils was found by interpolation. The same procedure was repeated for different body radius values between 5 cm and 25 cm. Figure 5.6 shows that, at any point of interest in the shaded area of the graph, the SNR of the loopless antenna dominates the UISNR of the external coil and this region is called the useful area of the loopless antenna. As a result, if the point of interest is in the shaded region, the loopless antenna should be used.

Comparing the loopless antenna with the UISNR of an internal and external coil combination allows a determination of how much improvement can be achieved over the loopless design, as well as determining the point of interest where the loopless antenna performs best. The intrinsic SNR values for the loopless antenna were divided by the UISNR of an internal and external coil combination and plotted as a function of the point of interest in Figure 5.7.

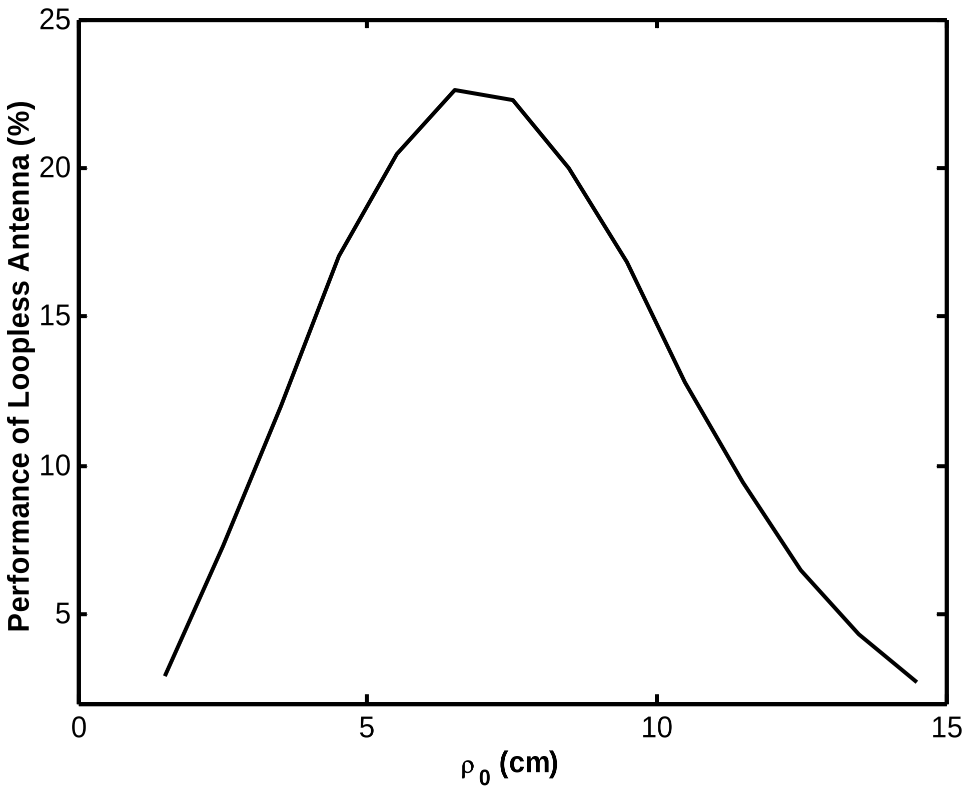

Figure 5.7: The performance of the loopless antenna as a function of distance of the point of interest from the center of the object. This figure was obtained by dividing the SNR of the loopless antenna by the UISNR of the internal and external coil combination. In this figure, a 20 cm body radius and a 0.375 mm cavity radius were assumed.

Our sample design loopless antenna achieved maximum performance at the points of interest with a distance to the center of the body around 6.5 cm $(\rho_0 = 6.5 \text{ cm})$. For those points, more than 20% of the maximum achievable SNR was obtained (see Figure 5.7).

5.4.4 Analysis of Endourethral Coil Design

The endourethral coil design (16) is an elongated single loop, which consists of a copper trace etched on a flexible circuit board. In order to calculate the intrinsic SNR values for the endourethral coil, a saline phantom experiment was conducted (FSE, ETL:64; TR/TE: 10000/22 msec; 256x256; 1 NEX; 3 mm slice; 32 cm FOV; BW: 62.5 kHz). Using the images of the phantom, the ISNR values were calculated as a function of radius for radial distances of 0.14 to 15 cm. The performance was measured by dividing the experimental ISNR value of this coil by the UISNR value. UISNR values were computed for a 20 cm radius body with an internal cavity radius of 2.5 mm (cavity size matched the endourethral coil diameter).

Experimental performance plots revealed that the performance of the single loop coil design reached 18% of its maximum and that there is still significant room for improvement in this design (see Figure 5.8). In addition, a comparison was made between the SNR of the single-loop endourethral coil and the UISNR value of external coils, i.e., with the case of no cavity. This comparison revealed that at the position of $(\rho = 1 \text{ cm}, \phi = 0, z = 0)$, the single-loop coil performs approximately 25 times better than any external coil.

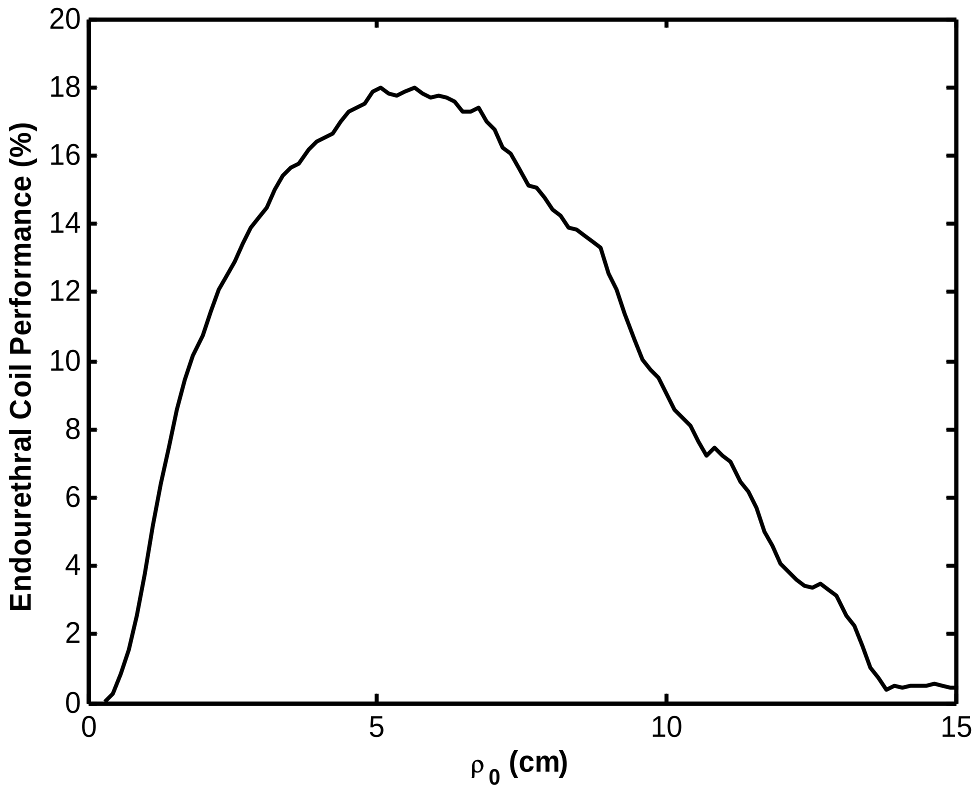

Figure 5.8: The experimental performance of the endourethral coil design as a function of distance of the point of interest from the center of the object. This figure shows the performance of a single-loop endourethral coil obtained by dividing the experimental SNR value of this coil by the UISNR of the internal coil. UISNR values were computed for a 20 cm radius body with an internal cavity radius of 2.5 mm (cavity size matched the endourethral coil diameter).

5.4.5 Parameters for UISNR

There are many parameters that affect the UISNR of internal coils, for instance, body radius ρ_b, cavity radius ρ_c, conductivity σ, relative electric permittivity ε_r, frequency ω, point of interest, and so forth. The point of interest was explored in detail in the previous section and frequency and cavity radius will be examined in this section.

One of the main factors for the UISNR that affects the SNR is frequency, which is directly proportional to the field strength. In Figure 5.9, various magnetic field strengths between 0.2 and 8.0 tesla were used in the plot. These values for magnetic field strengths (***B***) were chosen according to the values used for standard MRI systems. Quasi-static conditions are valid for regions near the boundaries where there is a linear relation between UISNR and the field strength. On the other hand, when the point of interest is away from the surface, UISNR increases faster with respect to frequency, as stated in (12). As frequency increases, the curvature of the curves becomes smaller. At 8 tesla, for the points of interest with radial distances from the center between 6 and 12 cm, the curve approaches a flat line. This behavior can be attributed to SNR gain due to focusing effects at high fields.

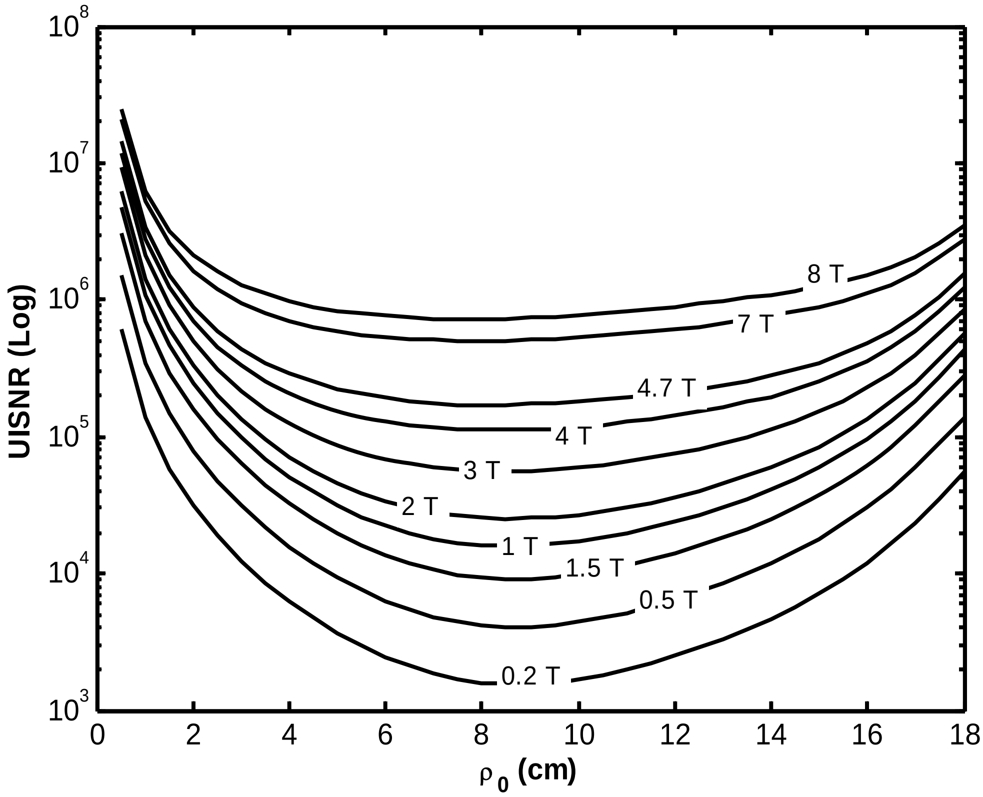

Figure 5.9: Frequency dependency of the UISNR at various magnetic field strengths. When the point of interest is at a small cylindrical radius, quasi-static conditions are valid and there is then an approximately linear relationship between the UISNR and field strength.

The cavity size is another important parameter for internal coils. The UISNR values for an internal coil were plotted for various cavity values and a 20 cm body radius (see Figure 5.10). The larger the cavity radius we used, the larger the SNR at points close to the center.

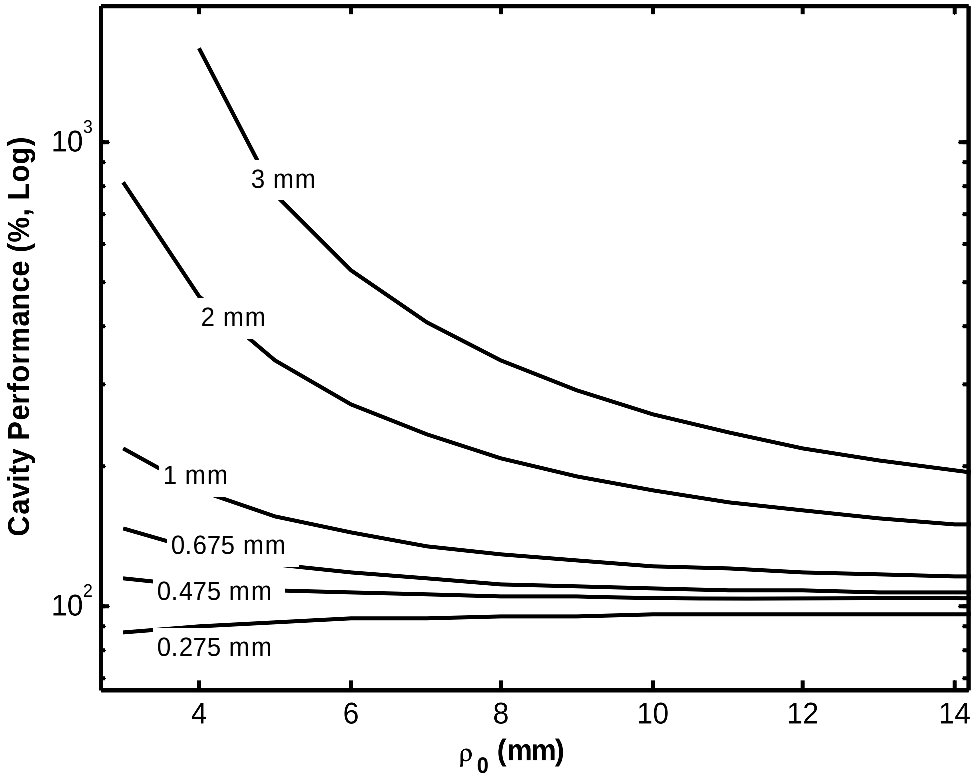

Figure 5.10: The performance of coils with different cavity sizes. In this figure, different UISNR values for internal coils were compared for different cavity sizes. The comparison was made by dividing the UISNR values of various coils, which have different cavity radii, to the UISNR value of the reference coil, which has a cavity radius equal to 0.375 mm

While making internal coil UISNR calculations, some other observations related to the use of internal coils were made. For example, the UISNR at a point of interest closer to the internal cavity was calculated for different body radius values and it was found that the UISNR value is weakly dependent on the body radius value. This shows that, for a region of points inside the human body, a well-designed coil should work with a similar performance, and is not strongly dependent on the size of the person to be imaged. This can be explained by the fact that the effect of the external coil is negligible for points closer to the internal cavity. Therefore, for this region, the position of the external coil (which depends on body size) does not really matter.

5.5 Discussion

Different field distributions can be obtained for different points of interest. It was observed that, as the point of interest gets closer to the outer boundary, the field distribution on the H-map becomes more effective (brighter) in the region close to the outer boundary. This can be explained by the fact that the internal coil loses its effect in that region. As a qualitative discussion, for the outer points, we can conclude that external coils are more suitable to obtain high SNR. Similarly, for the points of interest close to the internal cavity, the field was stronger at the inner regions. Therefore, for imaging inner points of the human body, internal coils are much more suitable. In addition, when a point of interest away from the origin is chosen, the H_f distribution of the field generated by the internal coil becomes uniform on the $\phi = 0$ plane. This is because the effect of the internal coil is very weak, and the optimum field produced by the internal coil does not change the UISNR significantly. However, as the point of interest approaches the inner region, the symmetry disappears and the internal coil field seems to be larger in magnitude.

Quasi-static conditions are effective when a point of interest is chosen at the region near the boundaries. In addition, as seen in Figure 5.9, linearity can be observed when the point of interest is at a small cylindrical radius, i.e., at the region very close to the cavity.

Mapping the field distribution can be a guide to the design of coils that have high SNR values close to the ultimate. In addition, the field distribution can roughly show the regions where the external and internal coils have negligible effects. For instance, for a point of interest where we obtain high field magnitudes near both the internal and external boundaries, both an internal and an external coil should be used to obtain an ultimate SNR value. For the maps, which show brightness only near the inner or outer boundaries, one type of coil would be enough.

The sagittal H-map (see Figure 5.3) was produced on the $\phi = 0$ plane with the point of interest $(\rho = 1\ \text{mm},\ \phi = 0,\ z = 0)$. In this figure, the highest brightness shows the position of the internal coil, located in the middle of the cylinder, in the z direction. At 1 mm or more away from the origin in the z direction, the field is very small with respect to the field at the center if we ignore some fluctuations caused by truncation. The amplitude of these fluctuations gets even smaller by increasing the truncation number, suggesting that the optimum internal coil that might produce such magnetic field distribution is smaller in length.

Another important point is the choice of a circular geometry. By using a cylindrical geometry, we were able to use a cylindrical wave expansion. This simplified our computational analysis. We were also able to add to our model a cylindrical cavity for the UISNR computation of internal coils, but in many medical applications for the internal coils, the body will not be circular and the cavity may not be centered.

Our sample designs, the loopless antenna and the endourethral coil, were found to be far from optimum. At least a 10-fold SNR improvement would be possible with another design. At this time, the geometry of the optimum coil design is unknown, but we believe that the results presented here will be useful in improving current coil designs and achieving the goal of determining the UISNR.

5.6 Conclusion

We have developed a method to calculate the ultimate value of the SNR that can be obtained with internal MRI coils. We propose to use this value as a reference to evaluate the performance of internal MRI coils. As an example, we have evaluated the performances of the endourethral coil and the loopless antenna, and assessed the extent of improvements required. In this work, cylindrical wave expansion, in which EM fields are represented by linear combinations of cylindrical waves, was used. In addition, we compared our results with experimental results. Our work can be used as a reference for the performance of internal coils as well as external coils.

6. MICROSTRIP BASED MR BIRDCAGE COIL FOR 1.5 T

6.1 Introduction

Birdcage is a well-known magnetic resonance (MR) head coil since it was firstly described in 1985 by Hayes et.al (8). It is widely used due to high signal to noise ratio and a high radiofrequency magnetic field homogeneity that guarantee a large field of view. Microstrip based birdcage coil for 4T is proposed in 2003 (46) and gives a very homogenous field. In this work, we analyze and fabricate microstrip based birdcage coil, which can be used as head coil for 1.5 Tesla MR imagers.

6.2 Method

In Figure 6.1, sectional sketch of a microstrip transmission line (MTL) can be seen: *H* is the distance between the strip conductor and the ground plane, *W* is the width of the strip, the strip-to-strip distance is given by *l*.

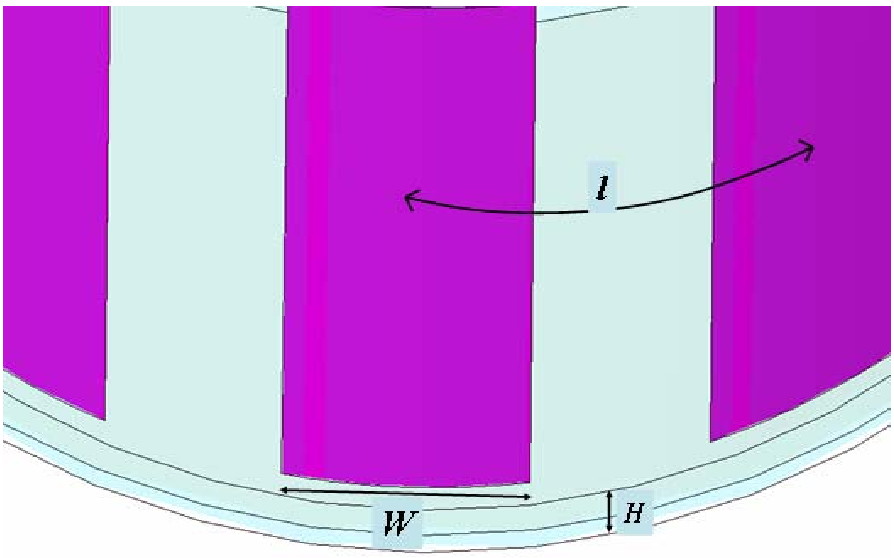

Figure 6.1: Sketch of Microstrip Based Birdcage Coil

Copper is commonly used for strip conductor and the ground plane. For the substrate we use acrylic with relative dielectric constant of 3.4. The geometrical and electrical properties of MTL determine the Q value, which is mainly dictated by radiation losses.

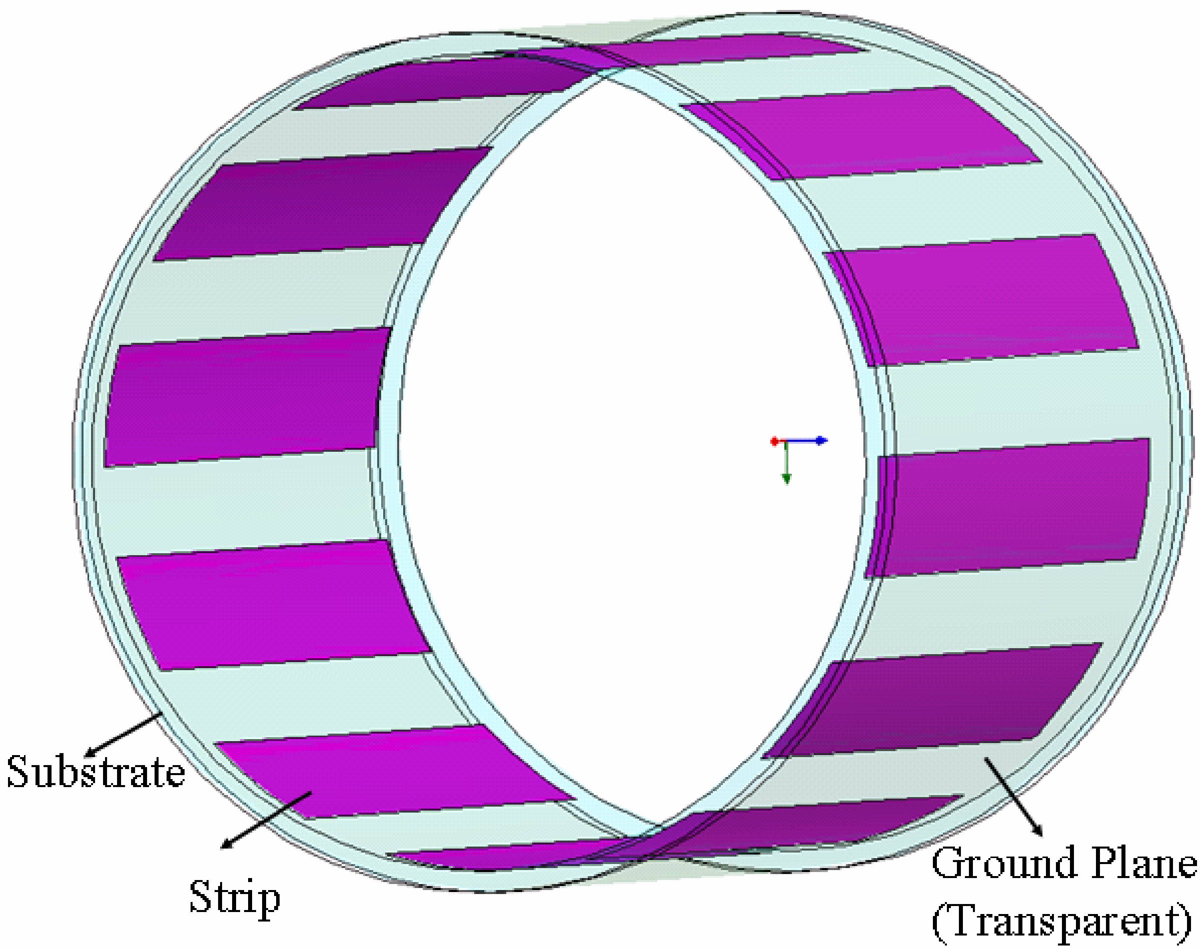

Figure 6.2: Another sketch of MSBC.

For the birdcage, shown in Figure 6.2, 12 microstrip lines are evenly distributed around the inner surface of a circular substrate. The outer surface is the ground plane. The strips are fed from one end and terminated by an open circuit at the other end. At the feeding end, lumped inductances are used for the tuning purpose. The equivalent circuit of the structure is obtained as a coupled resonant circuit. The resonant frequencies can be found from the strip capacitances and the lumped inductances. It is found that the first resonance is around 67 MHz, which is also found to be consistent with the experimental measurements. The slight differences may be attributed to the mutual inductances ignored in the analysis. This design has a low-pass characteristic. High pass structure can be obtained by short-circuiting the strip ends and using lumped capacitances between the strip lines at the feeding end.

6.3 Results

In Figure 6.3, built microstrip based birdcage coil can be seen.

Figure 6.3: A sketch of microstrip based birdcage coil for 1.5 T.

Below, resultant axial and sagittal images of gel-filled phantom are shown.

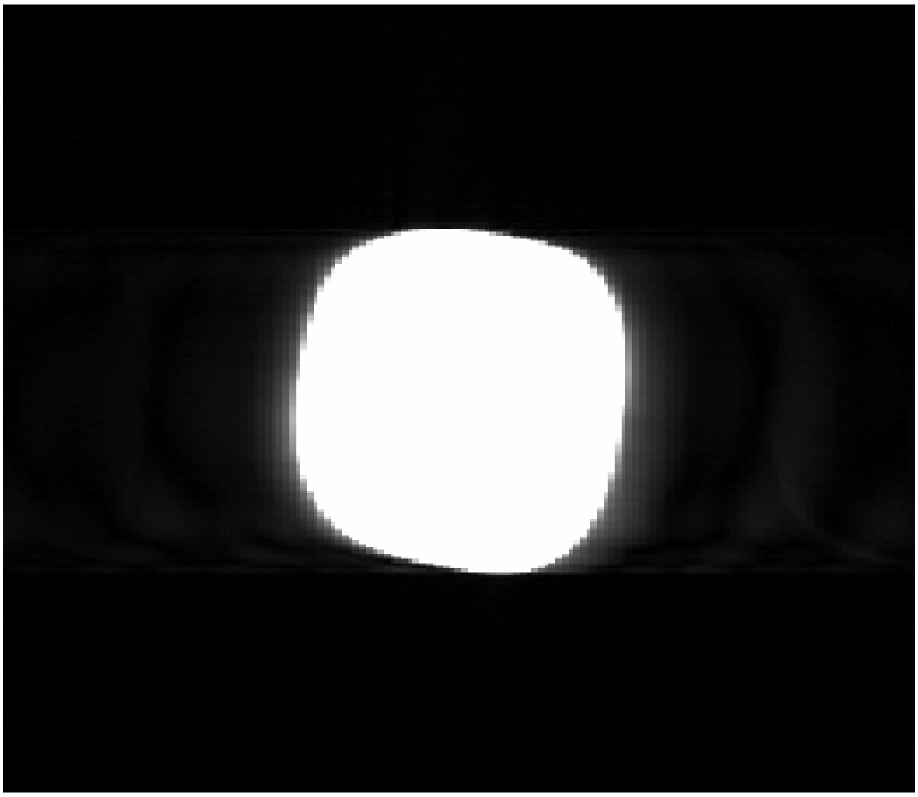

Figure 6.4: Axial Image of phantom

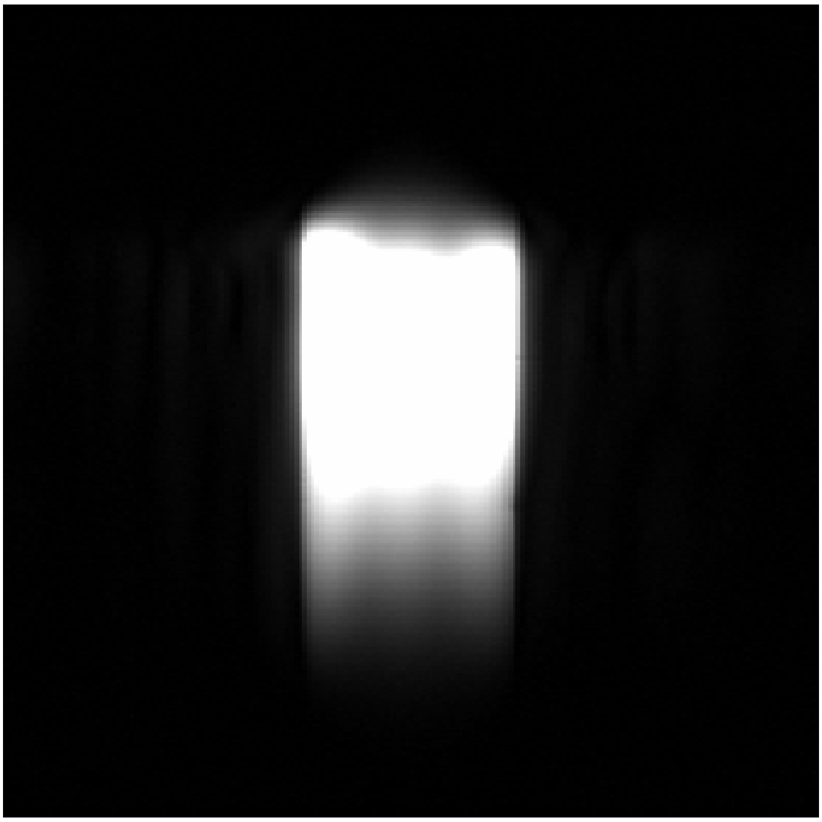

Figure 6.5: Coronal Image of phantom

6.4 Discussion

Field trapped inside microstrip can be manipulated easily. Using this idea may pave the way to improve ISNR of the birdcage coil. Our previous work (21) gave an idea about the optimum field that produces maximum achievable signal-to-noise ratio. As a future work, microstrip based birdcage will be rebuilt to obtain maximum possible SNR. In addition, the field structure is less dependent on the loading of the coil then conventional birdcage coil designs, so, transmit SENSE method can be implemented by the use of this microstrip based birdcage coil.

6.5 Conclusion

We fabricated microstrip based birdcage coil for 1.5 Tesla

7. FINISHING

Sophisticated RF technologies for MRI scanners are under development in order to increase effectiveness of diagnostic and interventional procedures. We believe, with the help of these novel technologies, interventionalists will be able to conduct very difficult procedures successfully and many lives will be saved.

There were two groups of studies in this thesis. The first group was on development of novel inductively coupled RF (ICRF) coil technologies for better device localization. In the first study, we showed that very straightforward manipulations on the data, which we called reverse polarization method, would provide very effective improvement on the catheter tracking procedures. Our second study was an extension of the first study for the phased array coils and this made the method more practical. In the third ICRF coil study, use of ICRF coil technology in image-guided neurosurgery was exploited as a registration marker by increasing the signal intensity of gel markers.

The second group of studies aimed to design optimum RF coil. We showed that there was still further room for improvement of the RF coils in order to obtain higher SNR images, which means higher resolution and more accurate diagnosis. In this study the ultimate value of any internal coil and required sensitivity for maximum SNR was calculated. By the use of sensitivity profile obtained from our theoretical studies it was shown that a specialized birdcage coil would generate optimum SNR and therefore we fabricated a microstrip based birdcage coil for 1.5 T imagers.

We plan to continue working on the novel RF coil technologies. Catheter tracking method will be implemented to a real-time procedure. In addition, more compact and low-cost markers will be designed. Furthermore, by a modifed microstrip technology, z-directed sensitivity of the birdcage coil will be manipulated to get even closer to the ultimate value of SNR .

Appendix A

The longitudinal components of the electric and magnetic field are given in Eqs. [14] and [15]. By applying these equations to Eq. [17], the other components of the electric and magnetic fields can be calculated as follows:

1) Electric Fields:

$$E_{\phi mn} = \left\{ \frac{m\beta_{zn}}{\rho\beta_{\rho n}^2}\left[A_{mn}J_m(\beta_{\rho n}\rho) + C_{mn}Y_m(\beta_{\rho n}\rho)\right] + \frac{\omega\mu}{\beta_{\rho \mathrm{n}}}\left[B_{mn}J'_m(\beta_{\rho n}\rho) + \mathrm{D}_{mn}Y'_m(\beta_{\rho n}\rho)\right]\right\} e^{jm\phi}e^{-j\beta_{zn}z}$$

[35]

$$E_{\rho mn} = \left\{ \frac{m\beta^2}{\sigma'\rho\beta_{\rho n}^2}\left[B_{mn}J_m(\beta_{\rho n}\rho) + \mathrm{D}_{mn}Y_m(\beta_{\rho n}\rho)\right] - \frac{j\beta_{zn}}{\beta_{\rho \mathrm{n}}}\left[A_{mn}J'_m(\beta_{\rho n}\rho) + \mathrm{C}_{mn}Y'_m(\beta_{\rho n}\rho)\right]\right\} e^{jm\phi}e^{-j\beta_{zn}z}$$

[36]

2) Magnetic Fields:

$$H_{\phi mn} = \left\{ \frac{-jm\beta_{zn}}{\rho\beta_{\rho n}^2}\left[B_{mn}J_m(\beta_{\rho n}\rho) + \mathrm{D}_{mn}Y_m(\beta_{\rho n}\rho)\right] - \frac{\sigma'}{\beta_{\rho \mathrm{n}}}\left[A_{mn}J'_m(\beta_{\rho n}\rho) + \mathrm{C}_{mn}Y'_m(\beta_{\rho n}\rho)\right]\right\} e^{jm\phi}e^{-j\beta_{zn}z}$$

[37]

$$H_{\rho mn} = \left\{ -\frac{m\beta^2}{\omega\mu\rho\beta_{\rho n}^2}\left[A_{mn}J_m(\beta_{\rho n}\rho) + \mathrm{C}_{mn}Y_m(\beta_{\rho n}\rho)\right] - \frac{\beta_{zn}}{\beta_{\rho \mathrm{n}}}\left[B_{mn}J'_m(\beta_{\rho n}\rho) + \mathrm{D}_{mn}Y'_m(\beta_{\rho n}\rho)\right]\right\} e^{jm\phi}e^{-j\beta_{zn}}$$

[38]

where $\sigma' = (\sigma + j\omega\varepsilon) = \dfrac{j\beta^2}{\omega\mu}$, and:

$$J'_m(\beta_{\rho n}\rho) = \frac{m}{\beta_\rho\rho}J_m\left(\beta_{\rho n}\rho\right) - J_{m+1}\left(\beta_{\rho n}\rho\right) \qquad [27]$$

$$Y'_m(\beta_{\rho n}\rho) = \frac{m}{\beta_\rho\rho}Y_m\left(\beta_{\rho n}\rho\right) - Y_{m+1}\left(\beta_{\rho n}\rho\right) \qquad [28]$$

Appendix B

The components of H_f can be calculated by using equation $H_f = \left(H_\rho - jH_\phi\right)/\sqrt{2}$ and Eqs. [37] and [38]. Using Eq. [20], the components of $\vec{\mathbf{b}}_{mn}\left(\vec{\mathbf{r}}\right) = \left[b_A, b_B, b_C, b_D\right]_{mn}$ can be evaluated as:

$$b_A\left(J_m, J_{m+1}\right) = \left[-J_m\left(\beta^2/\beta_\rho^2\right)\left(\sqrt{2}m/\omega\mu\rho\right) + J_{m+1}\left(\beta^2/\beta_\rho\right)\left(1/\left(\sqrt{2}\omega\mu\right)\right)\right]e^{jm\phi}e^{-j\beta_{zn}z}$$

$$b_B\left(J_m, J_{m+1}\right) = \left[-J_m\left(\beta_z/\beta_\rho^2\right)\left(\sqrt{2}m/\rho\right) + J_{m+1}\left(\beta_z/\beta_\rho\right)\left(1/\sqrt{2}\right)\right]e^{jm\phi}e^{-j\beta_{zn}z}$$

$$b_C\left(Y_m, Y_{m+1}\right) = \left[-Y_m\left(\beta^2/\beta_\rho^2\right)\left(\sqrt{2}m/\omega\mu\rho\right) + Y_{m+1}\left(\beta^2/\beta_\rho\right)\left(1/\left(\sqrt{2}\omega\mu\right)\right)\right]e^{jm\phi}e^{-j\beta_{zn}z}$$

$$b_D\left(Y_m, Y_{m+1}\right) = \left[-Y_m\left(\beta_z/\beta_\rho^2\right)\left(\sqrt{2}m/\rho\right) + Y_{m+1}\left(\beta_z/\beta_\rho\right)\left(1/\sqrt{2}\right)\right]e^{jm\phi}e^{-j\beta_{zn}z}$$

[29]

BIBLIOGRAPHY

1. Pruessmann KP, Weiger M, Scheidegger MB, Boesiger P. SENSE: Sensitivity encoding for fast MRI. Magnetic Resonance in Medicine 1999;42(5):952-962.
2. Wintersperger BJ, Nikolaou K, Dietrich O, Rieber J, Nittka M, Reiser MF, Schoenberg SO. Single breath-hold real-time cine MR imaging: improved temporal resolution using generalized autocalibrating partially parallel acquisition (GRAPPA) algorithm. European Radiology 2003;13(8):1931-1936.
3. Zerhouni EA. Mansfield Lecture: Strategic Directions and the Role of Imaging in 21st Century Healthcare: The NIH Perspective. 2006; Seattle.
4. Atalar E, Bottomley PA, Ocali O, Correia LCL, Kelemen MD, Lima JAC, Zerhouni EA. High resolution intravascular MRI and MRS by using a catheter receiver coil. Magnetic Resonance in Medicine 1996;36(4):596-605.
5. Kochli VD, McKinnon GC, Hofmann E, Vonschulthess GK. Vascular Interventions Guided by Ultrafast Mr-Imaging - Evaluation of Different Materials. Magnetic Resonance in Medicine 1994;31(3):309-314.
6. Ocali O, Atalar E. Intravascular magnetic resonance imaging using a loopless catheter antenna. Magn Reson Med 1997;37(1):112-118.
7. Quick HH, Zenge MO, Kuehl H, Kaiser G, Aker S, Massing S, Bosk S, Ladd ME. Interventional magnetic resonance angiography with no strings attached: Wireless active catheter visualization. Magnetic Resonance in Medicine 2005;53(2):446-455.
8. Hayes CE E, Schenck JF, Mueller OM, Eash M. An efficient, highly homogenous radiofrequency coil for whole-body NMR imaging at 1.5 T. J Magn Reson 1985;63.:622–628.
9. Çelik H, Atalar E. A Novel Catheter Tracking Method Using Reversed Polarization. 2005; Basle.
10. Çelik H, Ulutürk A, Eryaman Y, Talı T, Atalar E. A Novel Catheter Tracking Method Using Reversed Polarization. 2006; Seattle.
11. Zinreich SJ, Zinreich ES; IZI Corporation, assignee. Radiographic Multi-Modality Skin Markers. US patent 5,469,847. 1995 Nov. 28, 1995.
12. Ocali O, Atalar E. Ultimate intrinsic signal-to-noise ratio in MRI. Magn Reson Med 1998;39(3):462-473.
13. Edelstein WA, Glover GH, Hardy CJ, Redington RW. The intrinsic signal-to-noise ratio in NMR imaging. Magn Reson Med 1986;3(4):604-618.

14. Siemens. Total Imaging Matrix (TIM). 2006; Seattle.
15. Shunk KA, Lima JA, Heldman AW, Atalar E. Transesophageal magnetic resonance imaging. Magn Reson Med 1999;41(4):722-726.
16. Quick HH, Serfaty JM, Pannu HK, Genadry R, Yeung CJ, Atalar E. Endourethral MRI. Magn Reson Med 2001;45(1):138-146.
17. Kandarpa K, Jakab P, Patz S, Schoen FJ, Jolesz FA. Prototype miniature endoluminal MR imaging catheter. J Vasc Interv Radiol 1993;4(3):419-427.
18. Ocali O, Atalar E. Intravascular magnetic resonance imaging using a loopless catheter antenna. Magnetic Resonance in Medicine 1997;37(1):112-118.
19. Schnall MD, Imai Y, Tomaszewski J, Pollack HM, Lenkinski RE, Kressel HY. Prostate cancer: local staging with endorectal surface coil MR imaging. Radiology 1991;178(3):797-802.
20. Eryaman Y, Çelik H, Altıntaş A, Abdel-Hafez I, Atalar E. Evaluation of Internal Coils Using Ultimate Intrinsic SNR. 2003; Toronto.
21. Çelik H, Eryaman Y, Altintas A, Abdel-Hafez IA, Atalar E. Evaluation of internal MRI coils using ultimate intrinsic SNR. Magnetic Resonance in Medicine 2004;52(3):640-649.
22. Çelik H, Eryaman Y, Altintas A, Erturk VB, Atalar E. Microstrip Based MR Birdcage Coil for 1.5 T. 2005; Washington.
23. Çelik H, Eryaman Y, Altıntaş A, Erturk VB, Atalar E. Microstrip Based MR Birdcage Coil for 1.5 T. 2005; İstanbul.
24. Aksit P, Derbyshire JA, Serfaty JM, Atalar E. Multiple field of view MR fluoroscopy. Magnetic Resonance in Medicine 2002;47(1):53-60.
25. Lederman RJ, Guttman MA, Peters DC, Thompson RB, Sorger JM, Dick AJ, Raman VK, McVeigh ER. Catheter-based endomyocardial injection with real-time magnetic resonance imaging. Circulation 2002;105(11):1282-1284.
26. Hoult DI. The principle of reciprocity in signal strength calculations - A mathematical guide. Concepts in Magnetic Resonance 2000;12(4):173-187.
27. Çelik H, Ulutürk A, Eryaman Y, Talı T, E A. A Novel Catheter Tracking Method Using Reversed Polarization. 2006.
28. Silver X, Ni WX, Mercer EV, Beck BL, Bossart EL, Inglis B, Mareci TH. In vivo 1H magnetic resonance imaging and spectroscopy of the rat spinal cord using an inductively-coupled chronically implanted RF coil. Magn Reson Med 2001;46(6):1216-1222.
29. Edelstein WA, Hardy CJ, Mueller OM. Electronic decoupling of surface coil receivers for NMR imaging and spectroscopy. J Magn Reson 1986;67:156-161.
30. Schnell W, Renz W, Vester M, Ermert H. Ultimate signal-to-noise-ratio of surface and body antennas for magnetic resonance imaging. Ieee Transactions on Antennas and Propagation 2000;48(3):418-428.

31. **Kowalski ME, Jin JM, Chen J. Computation of the signal-to-noise ratio of high-frequency magnetic resonance imagers. Ieee Transactions on Biomedical Engineering 2000;47(11):1525-1533.**
32. **Martin AJ, Plewes DB, Henkelman RM. MR imaging of blood vessels with an intravascular coil. J Magn Reson Imaging 1992;2(4):421-429.**
33. **Hurst GC, Hua J, Duerk JL, Cohen AM. Intravascular (catheter) NMR receiver probe: preliminary design analysis and application to canine iliofemoral imaging. Magn Reson Med 1992;24(2):343-357.**
34. **Kantor HL, Briggs RW, Balaban RS. In vivo 31P nuclear magnetic resonance measurements in canine heart using a catheter-coil. Circ Res 1984;55(2):261-266.**
35. **Quick HH, Ladd ME, Hilfiker PR, Paul GG, Ha SW, Debatin JF. Autoperfused balloon catheter for intravascular MR imaging. J Magn Reson Imaging 1999;9(3):428-434.**
36. **Martin AJ, McLoughlin RF, Chu KC, Barberi EA, Rutt BK. An expandable intravenous RF coil for arterial wall imaging. J Magn Reson Imaging 1998;8(1):226-234.**
37. **Schnall MD, Lenkinski RE, Pollack HM, Imai Y, Kressel HY. Prostate: MR imaging with an endorectal surface coil. Radiology 1989;172(2):570-574.**
38. **Abdel-Hafez IA. UISNR in MRI by Optimizing EM Field Generated by Internal Coils. 2000; Ankara. Bilkent University.**
39. **Veselle H, Collin RE. The Signal-TO-Noise Ratio of Nuclear Magnetic-Resonance Surface Coils and Application to a Lossy Dielectric Cylinder Model 1. Theory. IEEE Transactions on Biomedical Engineering 1995;42(5):497-506.**
40. **Vesselle H, Collin RE. The Signal-to-Noise Ratio of Nuclear-Magnetic-Resonance Surface Coils and Application to a Lossy Dielectric Cylinder Model .2. The Case of Cylindrical Window Coils. Ieee Transactions on Biomedical Engineering 1995;42(5):507-520.**
41. **Hoult DI R, RE. The signal-to-noise ratio of the nuclear magnetic resonance experiment. J Magn Reson 1976;24:71-85.**
42. **Morse P, Feshbach H. Methods of Theoretical Physics. New York: McGraw Hill; 1953.**
43. **Balanis C. Advanced Engineering Electromagnetics. New York: Wiley; 1989.**
44. **Susil RC, Yeung CJ, Atalar E. Intravascular extended sensitivity (IVES) MRI antennas. Magnetic Resonance in Medicine 2003;50(2):383-390.**
45. **Serfaty JM, Yang XM, Foo TK, Kumar A, Derbyshire A, Atalar E. MRI-guided coronary catheterization and PTCA: A feasibility study on a dog model. Magnetic Resonance in Medicine 2003;49(2):258-263.**

46. Zhang X, Ugurbil K, Chen W. A microstrip transmission line volume coil for human head MR imaging at 4T. J Magn Reson 2003;161(2):242-251.